

# Experimental, numerical, and multi-objective optimization investigations on the energy absorption features of single- and bi-layer deep-drawn cups

Proc IMechE Part L:  
J Materials: Design and Applications  
0(0) 1–22

© IMechE 2020

Article reuse guidelines:

sagepub.com/journals-permissions

DOI: 10.1177/1464420720972431

journals.sagepub.com/home/pil



Mohammad A Ghasemabadian<sup>1</sup> , Mehran Kadkhodayan<sup>1</sup>   
and William Altenhof<sup>2</sup>

## Abstract

In this article, the energy absorption features of single- and bi-layer deep-drawn cups (S- and B-cups, respectively) under a quasi-static axial loading are investigated experimentally and numerically. The S-cups were made of 304L stainless steel and explosively welded B-cups were composed of aluminum and 304L stainless steel layers. A multi-objective optimization was performed on specific energy absorption and initial peak force based on the polynomial response surface method. Furthermore, to compare the energy absorption features of deep-drawn cups, two groups of 304L stainless steel tubes (with the same mass or the same height as the S-cups) were axially compressed. The experimental results indicated that the S-cups experienced total energy absorption and mean crush force approximately 24% and 51% greater than those of tubes with the same mass and thickness, respectively. Furthermore, the total efficiency and specific total efficiency of the S-cups were approximately 0.23 and 1.82 times greater than those of tubes with the same height and thickness. Moreover, the energy absorbing effectiveness factor of B-cups was approximately twice of the S-cup.

## Keywords

Crashworthiness features, single- and bi-layer deep-drawn cups, energy absorption, multi-objective optimization

Date received: 4 August 2020; accepted: 19 October 2020

## Introduction

According to the world statistics of road traffic deaths, totaling 1.35 million people per year,<sup>1</sup> it is important to consider ways to reduce this significant amount of deaths. The use of energy dissipation devices as bumpers, guide rails, and a plethora of other mechanical systems to protect vehicle occupants from injuries during road accidents is crucial. As widely used and perhaps the most researched energy dissipation device, thin-walled tubes can dissipate kinetic energy in different manners such as cyclic plastic deformation, plastic bending, fracture, metal cutting, and friction. Despite all their useful advantages such as high strength and stiffness, excellent loading-carrying efficiency, excellent energy absorption, and dissipation of energy associated with a colliding dynamic system in a controlled manner, these structures show an extremely high initial peak force (IPF) when subjected to axial impact which increases the possibility of serious damages or human injuries

and fatalities. Extensive studies have been done to reduce the peak crushing force and to enhance the crashworthiness performance of these life critical structures.<sup>2–4</sup> To this end, over the previous decade, many mechanisms to initiate a stable collapse mode, such as using triggers, pre-folded tubes, corrugated thin-walled tubes, thickness variation, bitubular methods, and thin-walled tubes with different cross sections have been proposed by researchers.<sup>5–8</sup>

To reduce the IPF and improve the collapse process, some studies have investigated the application of

<sup>1</sup>Department of Mechanical Engineering, Ferdowsi University of Mashhad, Iran

<sup>2</sup>Department of Mechanical, Automotive and Materials Engineering, University of Windsor, Canada

### Corresponding author:

Mehran Kadkhodayan, Department of Mechanical Engineering, Ferdowsi University of Mashhad, Mashhad, Iran.  
Email: kadkhoda@um.ac.ir

trigger mechanisms such as holes manufactured into the thin-walled tubes. Arnold and Altenhof<sup>9</sup> investigated the load management and energy absorption features of extruded aluminum alloy square tubes, without and with circular hole discontinuities under quasi-static compression loads. They reported that the peak crush force of tubes with circular discontinuities decreased approximately of 23% compared to tubes without these discontinuities.

Besides trigger mechanisms, applying grooved patterns on the thin-walled tubes is another method for enhancement the energy absorption features. Xu et al.<sup>10</sup> investigated a novel cutout groove pattern to improve the energy absorption performances of square tubes for subway vehicles. Based on their optimal results, they found that the IPF of grooved tubes decreased by 31% compared to traditional designs.

Corrugated tubes are widely used to control the energy absorption characteristics of sacrificial safety structures. Mahbod and Asgari<sup>11</sup> developed a new corrugation pattern to enhance the crashworthiness performances of foam-filled composite tubes subjected to quasi-static oblique and axial impact loadings. Their numerical results demonstrated that generation of corrugation on the surface of tubes resulted in a decrease of 53% on the IPF for the designs considered within their study. Wu et al.<sup>12</sup> studied the impact behavior of sinusoidal corrugated tubes to control the collapse mode and reduce the IPF. Their results showed that these tubes could make the deformation mode more predictable and controllable. Also, they reported that a 47–84% reduction of IPF was achieved in the corrugated tubes.

To improve the crashworthiness behavior of thin-walled tubes, some researchers investigated thickness variation within the extrusions. Inspired by the concept of thickness gradient within bamboo, Song et al.<sup>13</sup> investigated the energy absorption performances of variable thickness tubes under axial impact force, numerically and experimentally. They found that the IPF of variable thickness tubes was at least 28% less than conventional circular tubes.

As a solution for improvement of impact behavior of thin-walled tubes, some researchers focused on thin-walled bitubular systems. Crashworthiness behavior of bitubular energy absorbers consisting of two coaxial tubes with different diameters subjected to quasi-static axial force was studied experimentally by Sharifi et al.<sup>14</sup> Their results showed that, compared to the equivalent monotubular structures with the same mass, the IPF of bitubular entities was 68.3% less than that of monotubular specimens.

Hemispherical shells are other thin-walled structures which are widely used in energy dissipation applications for aerospace, defense, and automotive industries<sup>15</sup> due to their high energy absorbing capacity, more stable crush response, and lower initial peak load.<sup>16,17</sup> Exploiting the properties of low initial peak load of hemispherical thin-walled shells and the

superior energy absorption properties of thin-walled tubes, encouraged the researchers to study the energy absorption characteristics of the combined geometrics shells under quasi-static and impact loadings. These thin-walled structures are composed of a tubular wall and a hemispherical cap. Mechanical behavior of combined shells composed of a cylindrical segment and a hemispherical cap subjected to dynamic and quasi-static axial crushing loads was investigated by Tasdemirci et al.<sup>18</sup> They observed that an increase in specimen thickness increased the specific energy absorption (SEA) and mean crush force. Generally, with different material combinations, multi-layered structures can possess advantageous properties such as anti-corrosion properties, good thermal conductivity, surface quality and wear resistance, and so forth, which surpass those of single metal sheets. Some researchers studied the energy absorption characteristics of multi-layered cups to exploit the structural benefits for impact/crash mitigation. For example, Tsukamoto<sup>19</sup> studied impact compression mechanism of deep-drawn cups having duralumin/aluminum multi-layered graded structures and reported that the six-layer cups possessed great energy absorption features in addition to improved performance associated with peak force. Finally, by considering performance parameters including crush efficiency, SEA, mean crush force, crush force efficiency (CFE), specific total efficiency, and total efficiency, Ghasemabadian et al.<sup>20</sup> investigated the effect of apparatus, material, and geometric factors on the energy absorption features of single- and bi-layer cups subjected to quasi-static compressive loads, experimentally. They found that the cups behaved with two major energy absorption mechanisms due to their wall heights or deformation modes. Moreover, their results showed that the layering sequence had a significant influence on the energy absorption performances and observed that cups with an aluminum inner layer exhibited mean crush force 14% higher than that of structures with the stainless steel inner layer. Additionally, they showed that the cups made by explosive welding method exhibited advantages over the cups joint by adhesive and reported that explosive welded cups experienced SEA and mean crush force 1.5 times greater than those of adhesively bonded cups.

It is evident from the literature survey summarized above that information on the energy absorption response of single- and bi-layer cup structures is very circumscribed and there is no comprehensive comparison study between the energy absorption performances of combined geometry shells and circular tubes. Correspondingly, a comprehensive comparison between energy absorption features of cup structures and conventional tubes are original contributions in the current investigation. Moreover, the structural synergistic behavior of bi-layer cups, optimization of energy absorption characteristics of single-layer

cups as well as the investigation on the mechanical behavior of the inner and the outer layers of a bi-layer cup is another contribution of this study.

## Experimental testing procedure and numerical modeling

### Experiment testing procedure

**Specimens preparation and specifications.** In this study, the explosive welding process was applied to fabricate the bi-layer plates (Figure 1). A 6.8 kg mass of AMATOL powder (as the explosive material) was applied on the as-received AA3105-O aluminum alloy sheet to generate a detonation velocity of approximately 2300 m/s. This velocity enabled the AA3105 plate, as the flyer plate, to weld to the 304L stainless steel (as the base plate). The matching surfaces were polished and cleaned using a commercial paint thinner, and the distance between the base and the flyer plates was 3 mm. Moreover, to remove the distortions due to the explosion on the clad, a cold-rolling process was achieved and the final thickness of plates was reduced by approximately 5%. For a single-layer plate considered in this study, a 304L stainless steel plate of 1 mm thickness was selected. 304L stainless steel tubes were prepared with three different thicknesses and two diameters. To compare with deep-drawn cups, tubes were prepared in two methods, namely, with the same height and with the same mass as the cups. Hence, tubes were machined to the required height and mass.

Specifications of the cups and tubes are provided in Table 1. Bi-layer explosive welded cups and single-layer cups are signified as B-cup and S-cup, respectively. In the naming of tubes, three codes are used. From the left, the codes are used to identify the method, thickness, and diameter, respectively. In the first specimen ID, letter H represents the tubes with the same height as the S-cup (H-type tubes) while letter M demonstrates the tubes having the same mass as the S-cup (M-type tubes). In the next code, the numbers 1, 2, and 3 indicate the thickness of 1, 1.25, and 1.5 mm, and in the last code, numbers 1 and 2 represent the diameters of 51 and 63 mm, respectively. For example, H<sub>12</sub> represents tube specimen having

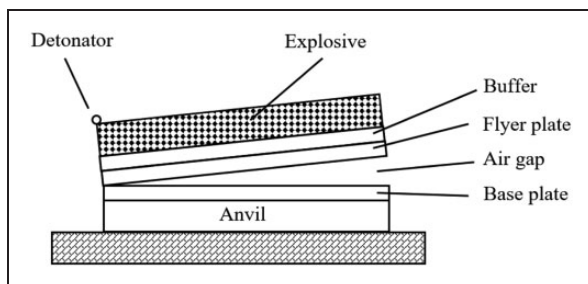


**Figure 1.** Schematic view of the experimental setup of the explosive welding process.

1 mm thickness and 63 mm diameter that has the same height as that of S-cups. Figures 2 and 3 illustrate a limited selection of the prepared cups and tubes, respectively.

**Deep-drawing procedure.** Circular blanks having a diameter of 140 mm were cut from the plates using a water jet machining technique and formed using a 60-ton hydraulic press and a die/punch/blank-holder set at the Ferdowsi University of Mashhad (which has been developed by the coauthors<sup>21</sup>) as presented in Figure 4.

To provide the blank-holder force, eight B/32/051 springs with stiffness and a free-length of 134 N/mm and 50 mm, respectively, were installed in an equally distributed manner around the surface of the blank holder. The forming process was performed at a punch speed of 9 mm/s and in the absence of any lubrication. The dimensions of tools used for the deep-drawing procedure as illustrated in Figure 5, are summarized in Table 2. Following the forming process, a lathe machining operation was completed by a professional machinist to trim the cup edge. The trimmed and un-trimmed cups are illustrated in Figure 6.

**Quasi-static test.** The quasi-static axial compressive tests were performed to study the energy absorption features and crushing mechanism of S- and B-cups. All experimental tests within this study were

**Table 1.** Geometric parameters and specifications of the specimens.

Specimen ID	Mass, $m$ (kg)	Height, $H$ (mm)	Thickness, $t$ (mm)	Diameter, $D$ (mm)
S-cup	0.0601	33.7	1	65.5
B-cup	0.0820	30	1.9	65.5
M <sub>11</sub>	0.0601	53.45	1	51
M <sub>12</sub>	0.0601	44.80	1	63
M <sub>21</sub>	0.0601	49.71	1.25	51
M <sub>31</sub>	0.0601	36.7	1.5	51
M <sub>32</sub>	0.0601	27.25	1.5	63
H <sub>11</sub>	0.0372	33.7	1	51
H <sub>12</sub>	0.0455	33.7	1	63
H <sub>21</sub>	0.0414	33.7	1.25	51
H <sub>31</sub>	0.0521	33.7	1.5	51
H <sub>32</sub>	0.0684	33.7	1.5	63

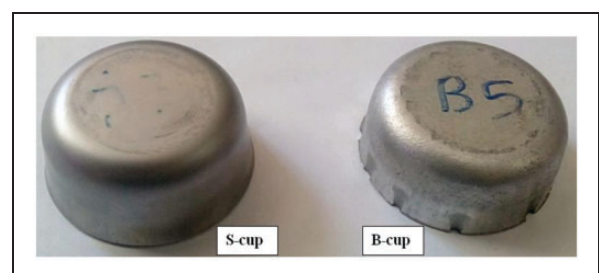


**Figure 2.** Prepared cups.



Figure 3. Some of the prepared tubes.



Figure 4. Sixty-ton hydraulic press and die set.

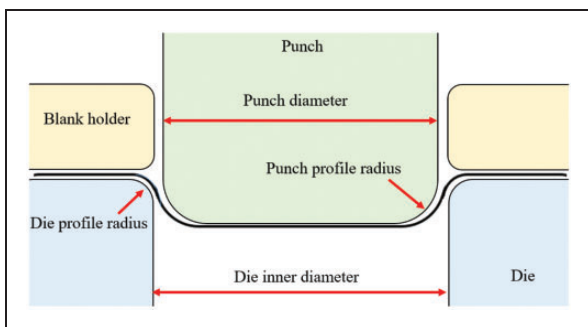


Figure 5. Schematic representation of the deep-drawing test.

Table 2. Dimensions of deep-drawing die set parts.

Dimension	Value (mm)
Die inner diameter	70
Punch diameter	65.5
Punch and die profile radius	5

conducted using a Universal Testing Machine made by the Zwick Company with a load cell having a capacity of 250 kN at the Ferdowsi University of Mashhad. The testing setup is shown in Figure 7.

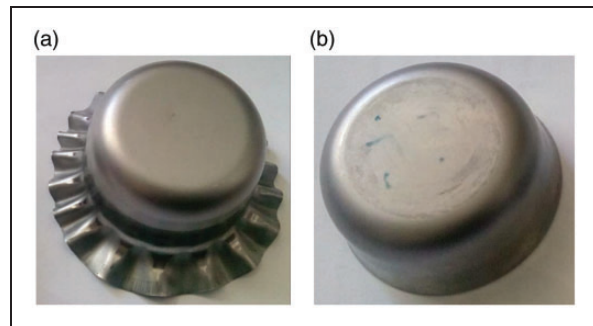


Figure 6. Formed cups: (a) before and (b) after trimming.

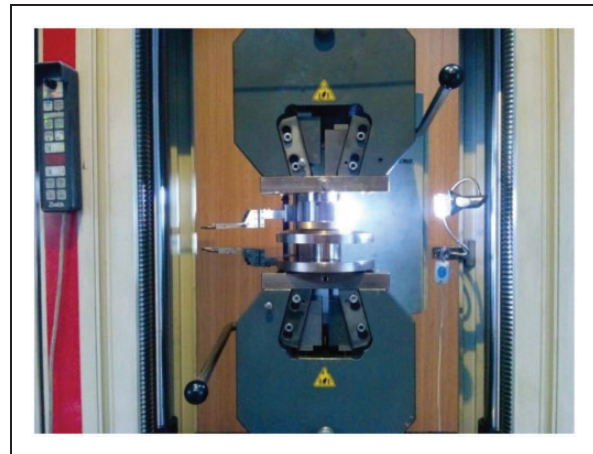
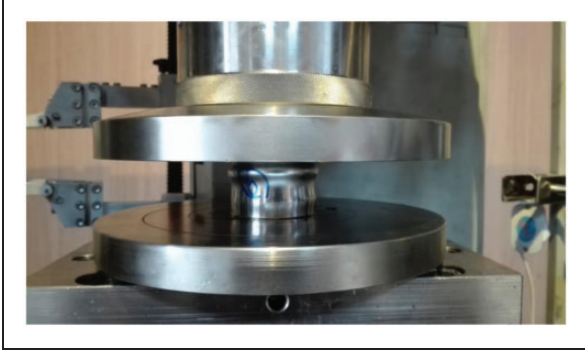


Figure 7. Testing apparatus.

A 75 mm extensometer was used to measure the displacement of the translating platform on the testing machine. A personal computer equipped with the testXpert III testing software was used to record the measurements of the compressive load and displacement.

A data sampling rate of 60 Hz was used for all quasi-static tests. During the crushing testing process, the specimens were deformed between the upper moving and lower stationary crossheads at a rate of 2 mm/min and no further fixturing was utilized to



**Figure 8.** Quasi-static axial crushing of a tube specimen.

hold the specimen (Figure 8). Furthermore, to assess the repeatability and to achieve better accuracy, at least three samples of each cup or tube were subjected to quasi-static axial compression loading.

### Structural crashworthiness criteria

**Total energy absorption ( $E_{abs}$ ).** Total energy absorption ( $E_{abs}$ ) is defined as the work done by the crush force during the process of deformation and obtained as the area under the force/displacement response, that is

$$E_{abs} = \int_0^{\delta} F(x)dx \quad (1)$$

where  $F(x)$  is the instantaneous axial crush force at a distance  $x$  in the axial direction and  $\delta$  is the effective deformation of specimen just prior to full compaction in testing and is determined as the onset of a sudden rapid increase in force within the force/displacement response (known as a “bottoming-out” phenomenon). Mathematically, the effective deformation is considered as the compression displacement corresponding to the maximum value of the deformation efficiency  $f$  which is defined as the following equation<sup>22</sup>

$$f = \frac{E_{abs}}{F_{max}} \quad (2)$$

where  $F_{max}$  denotes the maximum crush force in the interval  $[0, d]$ , excluding  $F_{peak}$  and  $d$  is the total crushing displacement experienced in the crushing test. Figure 9 demonstrates the effective deformation. In this study, to obtain the total energy from the experimental results, the trapezoidal rule is utilized as indicated in equation (3) for numerical integration of equation (1)

$$E_{abs} = \frac{1}{2} \sum_{i=1}^{n-1} [f(x_{i+1}) - f(x_i)] \cdot [x_{i+1} - x_i] \quad (3)$$

**Initial peak force ( $F_{peak}$ ), peak crush force ( $F_{max}$ ), and displacement.** For practical applications, the IPF is the predominant parameter in evaluating the crashworthiness performance of energy absorbers. The IPF ( $F_{peak}$ )

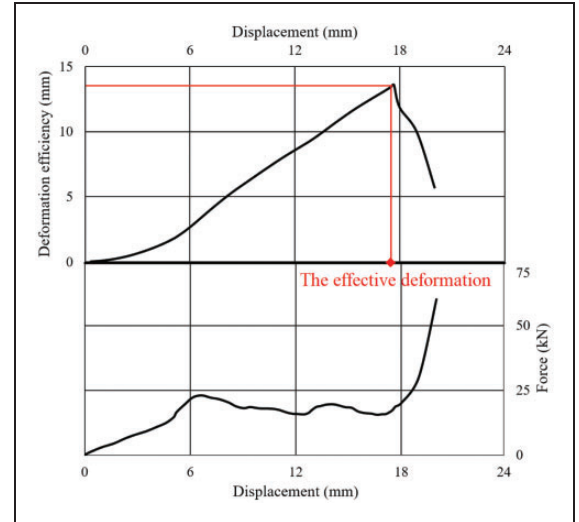


**Figure 9.** Deformation efficiency/displacement and force/displacement responses of a typical cup.

occurs due to the yielding of the material. Usually, it is preferable that this value is equal to the mean crushing force to avoid significant fluctuations in load transmission to other structures and occupants<sup>23</sup> resulting in levels of acceleration which may induce significant trauma or death. Energy dissipation structures with deformation characteristics which can suitably alter acceleration/time responses to improve crash performance are critical in engineering of protective structures. For example, when examining trauma in the brain, through measurement of strain, for various acceleration/time responses exhibiting the same peak acceleration and duration where the peak value occurred early (advanced) or later (delayed) in the time domain, Saboori et al.<sup>24</sup> observed strains in the brain being a function of the time to peak acceleration. The magnitude of strain in the brain depended on the profile of the acceleration/time response and it was reported that larger strains, and thus more significant brain trauma, were observed for an advanced peak value of acceleration. Hence, to reduce the initial deceleration which occupants and/or structures may be subjected to, it is desirable that  $F_{peak}$  occurs later in the time or displacement domain of applied load.<sup>25</sup> Moreover, for most thin-walled structures, the first peak force ( $F_{peak}$ ) is larger than the other local peak forces ( $F_{max}$ ). From the viewpoints of energy absorption and safety, the local peak forces are less important than the IPF, however, decelerations during the crash are created by these initial and local peak forces. Therefore, the crushing force should be maintained as constant as possible during deformation.<sup>26</sup>

**Mean crush force ( $F_{mean}$ ).** Mean crush force ( $F_{mean}$ ) is computed as the ratio of total energy absorption to the effective deformation  $\delta$

$$F_{mean} = \frac{E_{abs}}{\delta} \quad (4)$$

**Crush force efficiency.** CFE is found by the division of mean crush force by peak crush force as

$$\text{CFE} = \frac{F_{\text{mean}}}{F_{\text{max}}} \quad (5)$$

It is desirable that the CFE for energy absorbers is equal to unity to ensure no fluctuations in load during deformation.<sup>27,28</sup>

**Specific energy absorption.** SEA is known as one of the most important criteria to compare the energy absorption efficiency of structures when the weight reduction is vital and is calculated as the ratio of total energy absorption to the mass of the non-deformed structure

$$\text{SEA} = \frac{E_{\text{abs}}}{m} \quad (6)$$

This parameter helps designers to select the structure with the most amount of absorbed energy per unit mass.

**Crush efficiency or stroke efficiency ( $S_E$ ).** The crush efficiency is known as the ratio of the maximum shortening to the original length of the structure as

$$S_E = \frac{\delta}{L} \quad (7)$$

This non-dimensional criterion indicates the amount of structure length which is deformed and used up in the event of a crash. Hence, it is a main indicator for the applications with space limitation. Moreover, higher amounts of crush efficiency result in a decrease in the average value of transferred force to the occupants and equipment<sup>29</sup> due to the work done by the crushing force.

**Total efficiency ( $T_E$ ).** Total efficiency is obtained as the product of stroke efficiency and the CFE as<sup>22</sup>

$$T_E = (S_E) \cdot (\text{CFE}) \quad (8)$$

**Specific total efficiency ( $T_E^*$ ).** Specific total efficiency ( $T_E^*$ ) is obtained by division of total efficiency ( $T_E$ ) by mass of the undeformed structure as

$$T_E^* = \frac{T_E}{m} \quad (9)$$

This criterion is known as the most comprehensive criterion due to the nature of incorporating mass, means crush force, peak force, and stroke efficiency as

$$T_E^* = \frac{S_E F_{\text{mean}}}{m F_{\text{max}}} \quad (10)$$

**Energy absorbing effectiveness factor  $\psi$ .** Energy absorbing effectiveness factor ( $\psi$ ) is defined as the ratio of the total plastic and elastic strain energy absorption by a structure to the maximum absorbed energy of a material with the same volume up to failure in a standard normal tensile test.<sup>30</sup> This dimensionless parameter is utilized to compare the performances of the energy dissipation structures for different materials and combinations.<sup>31</sup>

### Numerical modeling

To better understand the deformation behavior that leads to energy absorption, the deep-drawing process and springback phenomenon as well as the quasi-static compression of single- and bi-layer cups made of stainless steel 304 and aluminum 3105 (namely, S- and B-type) were modeled using ABAQUS/Explicit.

**Deep-drawing process simulation.** As the blank showed minor wrinkle imperfections after deep-drawing process, the simulations were considered in full geometry. The deep-drawing model consisted of blank, punch, blank holder, and die as shown in Figure 10(a). The die, the punch, and the blank holder were considered as rigid bodies by four-node 3D elements type R3D4, while the bi-layer blank was modeled using five C3D8R elements through the thickness of each layer (eight-node linear brick elements with one reduced Gaussian integration point and stiffness hourglass control with the default hourglass scaling factor of 1).<sup>32,33</sup> Contacts between blank–blank holder, blank–punch, and blank–die were modeled as surface-to-surface.

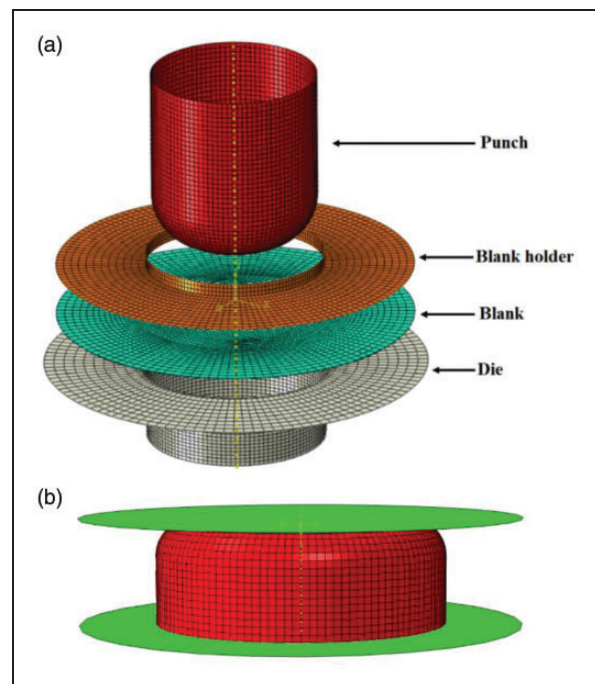


**Figure 10.** Finite element model: (a) deep drawing and (b) crushing.

**Springback simulation.** Since the accuracy of forming parts and accordingly the quasi-static compression results are affected by the springback phenomenon and its residual strain and stress fields, it is essential to predict the springback in the Finite Element (FE) modeling. To model the springback phenomenon, a new FE model was copied from deep-drawing model. In this model, all rigid components, namely the punch, the die, and the blank holder were removed. Moreover, since springback is a static simulation without external contact or/and loading, Abaqus/Standard can obtain a springback solution in just a few increments and is much more effective than dynamic/explicit. Therefore, dynamic/explicit method was replaced by static/implicit. All the remaining boundary conditions and interactions (namely, surface-to-surface contact and friction) of deep-drawing modeling were removed and the node at the cup center was fixed in the axial direction. The deep-drawing results including the displacement, strain, and stress history of elements were recalled and assigned to the bi-layer blank elements as a pre-defined field. Finally, in this step, artificial stresses that equilibrate the imported stresses are applied automatically by static/implicit and gradually eliminated during the step. The obtained displacement and stresses at the end of the step are the springback and residual stress, respectively.

**Quasi-static axial compression simulation.** As illustrated in Figure 10(b), three parts were considered in the FE model of quasi-static compression: the rigid top plate as the moving plate, the rigid bottom plate as the base and the cup which was input from the springback model. Furthermore, general contact was set in three models with the friction coefficient value of 0.3, which was obtained in previous experimental studies.<sup>21</sup> Moreover, a mesh-sensitivity analysis was conducted to investigate the influence of mesh discretization on the numerical observations. To this end, the deep-drawing and quasi-static compression loading numerical models with mesh sizes of 6, 4, 3, 2, and 1 mm were considered. Figures 11 and 12 show

the mesh-sensitivity analysis for deep-drawing and low-velocity impact numerical modeling, respectively. The findings reveal that the mean crushing force in the quasi-static compression modeling and the total energy in deep-drawing simulation of mesh sizes of 1 and 2 mm differ only by 2–4%, hence, the optimum element size was determined to be 2 mm and accordingly was implemented into the modeling strategy. As the explosive zone was extremely thin and had no considerable effect on the energy absorption capability and no separation was observed during the deep-drawing and compression processes, it was ignored in the deep-drawing model.

Furthermore, a “Node-to-Surface” contact definition was established between the bottom plate and edge of the cup. Additionally, the top plate could move only in the axial direction, while the rigid bottom plate was fully constrained. All real structures possess geometric imperfections which are deviations from the perfect structure due to the production process or material imperfections.

In this study, the cups experienced the deep-drawing process which led to some imperfections. Since the numerical simulations cannot predict the asymmetric collapse modes due to perfect structure and material modeling, it is therefore essential to introduce some initial geometric imperfections to the cup model. To this end prior to the quasi-static simulation, the cup placed between two rigid plates was subjected to a buckling to obtain the first 100 buckling modes and their related Eigenvalues using ABAQUS/Standard. Then, the IMPERFECTION keyword was applied to recall the buckling modes from the input file. After that, buckling modes were scaled by predefined magnitudes (0.01 of the cup thickness) and finally, a linear combination of buckling modes with scale factors was considered as the geometry imperfection. To consider residual stress and strain fields as a result of the springback phenomenon and deep-drawing process, a predefined field option in ABAQUS/Explicit was applied to map these fields in the quasi-static model. An elastic–plastic model in conjunction with isotropic hardening and von Mises yield criterion available in ABAQUS

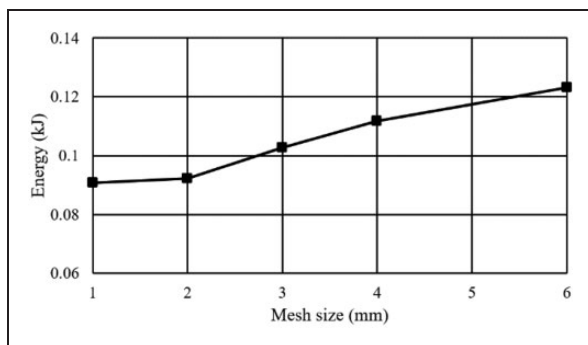


**Figure 11.** Mesh-sensitivity analysis for deep-drawing modeling.

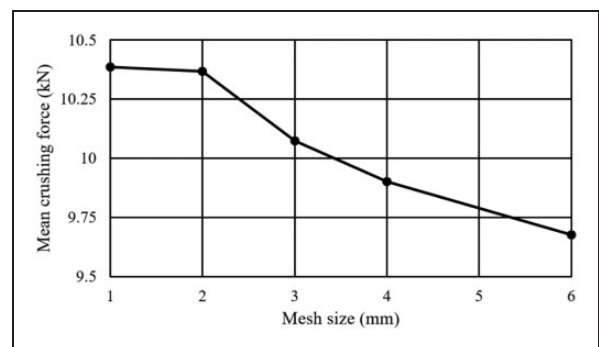


**Figure 12.** Mesh-sensitivity analysis for crushing modeling.

material library ( $J_2$ -plasticity) was used to simulate the mechanical properties of stainless steel 304 and aluminum 3105. The model is frequently used to simulate elastic–plastic metal deformation behavior and can be used for rate-dependent/independent materials.<sup>34</sup> To provide the necessary data into the material model, tensile testing was completed in accordance to ASTM E8-04<sup>35</sup> using a Universal Testing Machine with an extension rate of 2 mm/min. To ensure data repeatability, at least three tests were completed, which exhibited excellent consistency in mechanical material stress–strain behavior. For brevity, a representative true stress–true effective plastic strain response for each material, namely, the 304L stainless steel and aluminum 3105-O, is shown in Figure 13, from the testing undertaken. Moreover, the material properties of the aluminum alloy and 304L stainless steel are listed in Table 3. The yield strength of all materials was determined using a 0.2% offset strain method.

### Multi-objective optimization for cup shells

**Design methodology.** Cup shells, as an energy absorber, are expected to absorb as much crash energy per unit mass as possible. Furthermore, as previously indicated, the IPF is a critical force which may lead to severe irrecoverable injuries or death of occupants and should be reduced as much as possible. For these reasons, in this study, minimizing the IPF and maximizing SEA were considered as the optimization objectives. Moreover, various parameters affect the energy absorption of cup shells. Ghasemabadian and Kadkhodayan<sup>36</sup> showed that among all of them, four geometric parameters, namely, height,  $H$ ; specimen thickness,  $t$ ; diameter,  $D$ ; and corner radius of the cup,  $r$ , had the most effect on the IPF and SEA, therefore, these parameters were selected as design parameters. The range of constraint values of the design parameters was determined according to practical engineering applications and geometry limitations. Two deterministic multi-objective optimization

problems are formulated mathematically as equations (11) and (12)

$$\text{Type 1 : } \begin{cases} \max\{\text{SEA}, -\text{IPF}\} \\ \text{s.t. } 0.5 \text{ mm} \leq t \leq 1 \text{ mm} \\ 5 \text{ mm} \leq r \leq 15 \text{ mm} \\ 50 \text{ mm} \leq D \leq 70 \text{ mm} \end{cases} \quad (11)$$

$$\text{Type 2 : } \begin{cases} \max\{\text{SEA}, -\text{IPF}\} \\ \text{s.t. } 20 \text{ mm} \leq H \leq 40 \text{ mm} \\ 5 \text{ mm} \leq r \leq 15 \text{ mm} \\ 50 \text{ mm} \leq D \leq 70 \text{ mm} \end{cases} \quad (12)$$

**Polynomial response surface method.** Optimization techniques require mathematical formulation to calculate optimal states of the design. In the experimental and numerical studies, it is complicated to derive an analytical formulation from obtained data which describes the behavior of a criterion with respect to some parameters. To obtain a mathematical expression for optimization objectives, namely, SEA and IPF, the polynomial response surface method (PRSM) was used. In this method, an approximation  $\hat{y}(\chi)$  to the structural responses is considered in terms of the simple basis functions in a form of equation (13)

$$\hat{y}(\chi) = \sum_{j=0}^n a_j \varphi_j(\chi) \quad (13)$$

where  $\hat{y}$  is the response vector found by numerical simulation,  $\chi$  is the vector of design variables, and  $n$

**Table 3.** Material properties for the aluminum and stainless steel alloys.

Material	Material properties			
	$\rho$ (kg/m <sup>3</sup> )	$E$ (GPa)	$\sigma_y$ (MPa)	$\nu$
Al 3105	2700	68.1	57.5	0.33
304 SS	7800	210	310.4	0.3

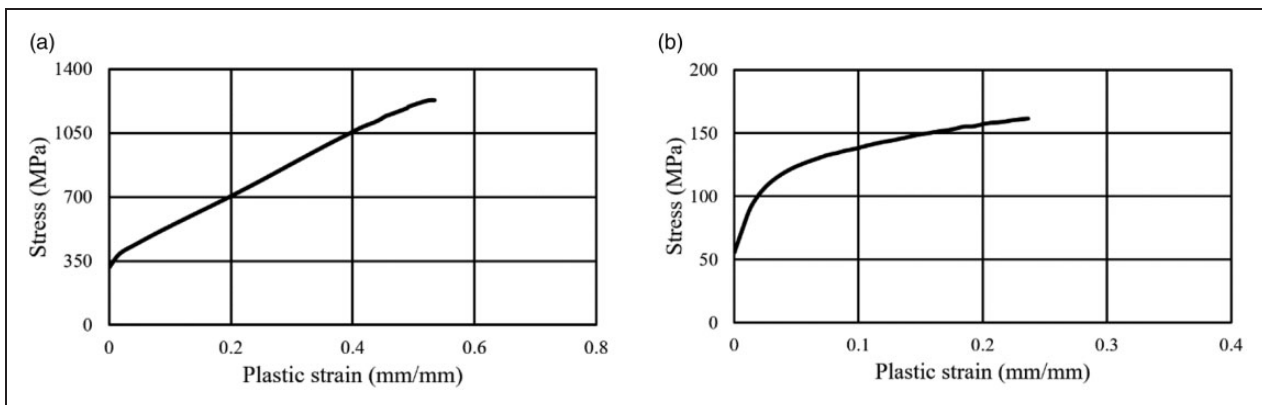


**Figure 13.** True stress–plastic strain behavior: (a) 304L stainless steel and (b) aluminum 3105.



is the order of polynomial function  $\varphi_j(\chi)$ . Usually, the polynomial function is considered as the basis function. In the matrix form, equation (13) may be expressed as equation (14)

$$\hat{Y} = A\Phi \quad (14)$$

where the vector of unknown coefficients  $A$  is solved using the method of least squares as equation (15)

$$A = (\Phi^T\Phi)^{-1}(\Phi^T y) \quad (15)$$

## Results and discussion

### Experimental findings

**Energy absorption features.** In general, energy absorption performances of thin-walled structures can be compared in several ways according to their wide range applications. Therefore, various quantitative criteria have been used to quantify crashworthiness and energy absorption efficiencies of these structures. The most important characteristic of an energy dissipation structure is its force/displacement response which quantitatively and qualitatively describes its crushing behavior, including the mechanical behavior and deformation mode of the energy absorber. Using this information, further assessment of the capabilities of the structure can be obtained, including, but not limited to, total absorbed energy, mean crush force, SEA, CFE, crush efficiency, total efficiency, specific total efficiency, and energy absorbing effectiveness factor. The values of the energy absorption characteristics obtained for specimens within this study are presented in Table 4.

The energy absorption features associated with S-cup (displayed in gray shading) are considered as the reference values, representing the baseline configuration of all cup specimens. Additionally, the relative percentage difference (RDP) values, using observations from the reference specimens, are calculated as

stated in equation (16), where  $P$  and  $R$  are the specimen and reference observation values, respectively

$$RDP = \frac{(P - R)}{R} \cdot 100\% \quad (16)$$

To provide an appropriate presentation of results and to understand the collapse progress of presented samples, the force/displacement responses of specimens with the same diameter and thickness are provided in five groups namely 11, 12, 21, 31, and 32 in Figure 14. For brevity, only one representative response from all tested samples is presented in Figure 14. In general, the deformation process of tubes begins with a sharp rise in force over a small range of deformation length. This sharp rise continues to the yield point when the tube material yields and the first peak force is created. After this point, the force drops dramatically due to the occurrence of a side wall fold following with progressive deformation in which folds are formed in the height of the tube and local peak forces are formed in the force/displacement response.<sup>37</sup>

Unlike the tubes, the cups behave differently, specifically, the force rises slowly and the displacement at which the peak force occurs is larger compared to that of tubes. Furthermore, in the case of cups, the first peak force indicates the buckling of the cup head and the following peaks are due to the formation of folds in the cup wall. Referring to Figure 14, it can be seen that for all tubes the first peak force occurred after approximately 2–3 mm of deformation while for S- and B-cups, they occur after approximately 11 and 12 mm, respectively. Furthermore, for all H-type tubes with the exception of H<sub>31</sub> specimen, the crush length is lower than that of M-type specimens due to their low heights. The initial heights of H<sub>31</sub> and M<sub>31</sub> (group 31) are nearly equal (33.7 and 36.7 mm, respectively), as indicated in Table 1. Additionally, the difference between forces of all groups is less than 5% after the first peak force at each displacement, with the exception of tubes within group 31 where this difference exceeds 50%. A comparison of

**Table 4.** Energy absorption features of tubes and cups.

No.	$E_{abs}$ (kJ)	$F_{max}$ (kN)	SEA (kJ/kg)	$F_{mean}$ (kN)	$S_E$	CFE	$T_E$	$T_E^*$ (1/kg)	$\psi$ ( $\times 10^3$ )	$\delta_P$ (mm)
S-cup	1.14	66.7	18.9	45.9	0.738	0.688	0.508	8.39	1.437	22.5
B-cup	1.33	113.1	16.2	68.9	0.641	0.608	0.390	4.75	2.636	13.1
M <sub>11</sub>	0.862	57.5	14.3	22.5	0.718	0.392	0.281	4.68	1.085	1.82
M <sub>12</sub>	1.24	88.5	20.6	35.2	0.746	0.398	0.313	5.20	1.564	1.95
M <sub>21</sub>	0.950	64.1	15.7	26.9	0.709	0.419	0.297	4.93	1.196	1.80
M <sub>31</sub>	1.37	99.6	22.7	55.6	0.670	0.558	0.374	6.20	1.723	2.19
M <sub>32</sub>	1.21	125.0	20.0	63.0	0.705	0.502	0.354	5.84	1.524	2.56
H <sub>11</sub>	0.684	83.0	18.4	32.1	0.632	0.387	0.245	6.57	0.862	1.82
H <sub>12</sub>	0.785	84.1	17.3	34.1	0.680	0.406	0.276	6.07	0.989	1.74
H <sub>21</sub>	0.546	65.6	13.2	26.9	0.600	0.410	0.246	5.94	0.687	1.64
H <sub>31</sub>	0.961	84.5	18.4	39.9	0.715	0.472	0.337	6.48	1.211	2.29
H <sub>32</sub>	1.28	112.2	18.7	54.1	0.701	0.482	0.338	4.94	1.612	2.34

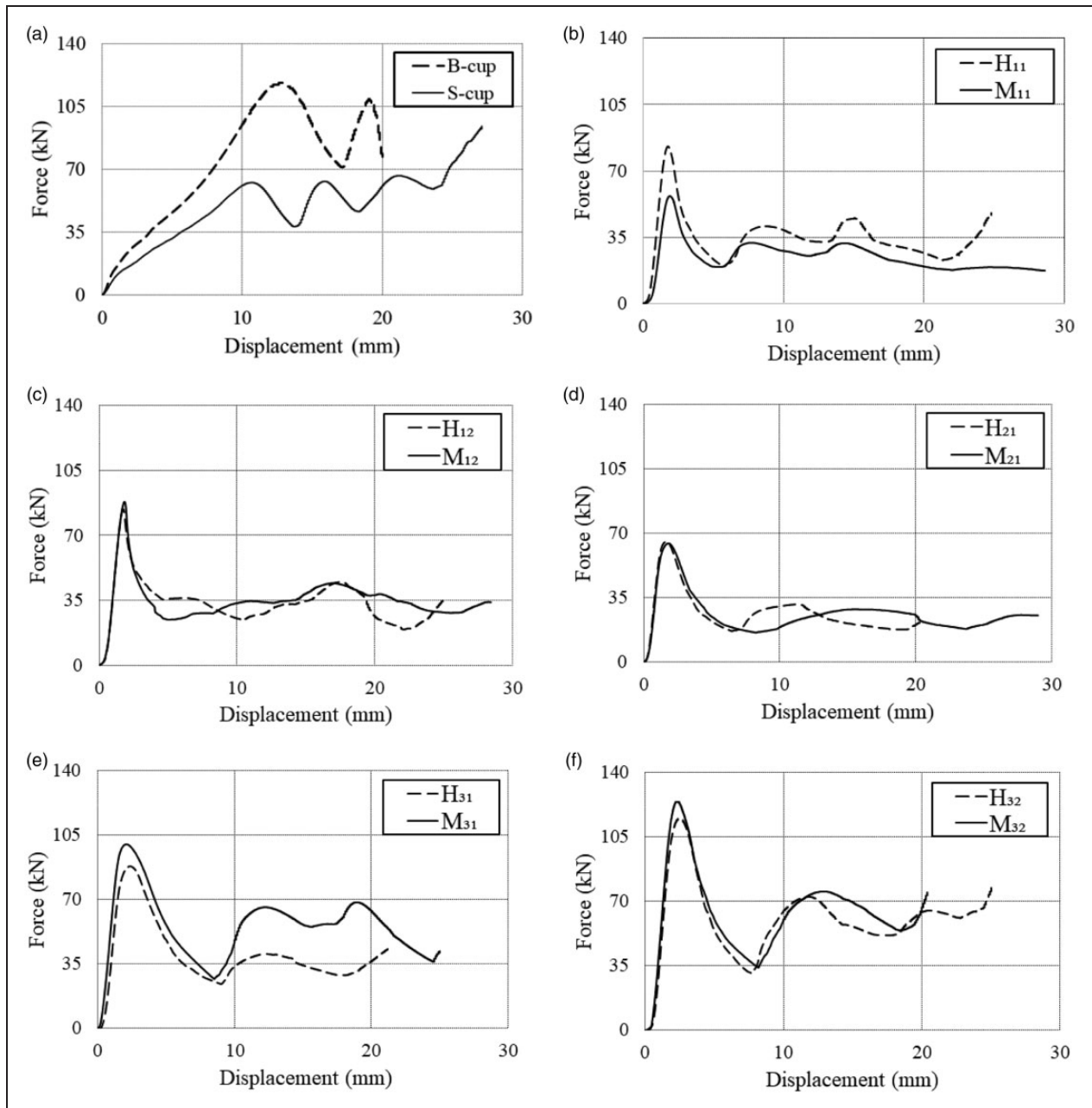


**Figure 14.** Force/displacement responses. (a) B- and S-cups. (b) Tubes with the same thickness of 1 mm and diameter of 51 mm (group 11). (c) Tubes with the same thickness of 1 mm and diameter of 63 mm (group 12). (d) Tubes with the same thickness of 1.25 mm and diameter of 51 mm (group 21). (e) Tubes with the same thickness of 1.5 mm and diameter of 51 mm (group 31). (f) Tubes with the same thickness of 1.5 mm and diameter of 63 mm (group 32).

the maximum peak force of all groups indicates that the highest and the lowest values of the maximum peak force belong to  $M_{32}$  and  $M_{11}$ , respectively. Moreover, the maximum peak force of H- and M-types of groups 12 and 21 is nearly the same. According to Figure 14(a), B- and S-cups experienced two and three local peak forces, respectively. As previously indicated, these peak forces accompany the formation of additional folds in the deformation process.

Furthermore, the crush length of S-cup was observed to be more than that of B-cup due to a greater initial height of the S-cup, that being

approximately 4 mm more than that of the B-cup. The first column of Table 4 demonstrates that B-cup absorbs more energy than S-cup by approximately 17%. For tubes having the same mass as S-cup,  $M_{31}$  absorbs energy more than the reference cup approximately 0.23 kJ, while the total energy absorption of  $M_{11}$  and  $M_{21}$  is approximately 17% and 24% less than that of S-cup. Furthermore, all H-type tubes exhibit less  $E_{abs}$  than S-cup except for  $H_{32}$  which absorbs more energy than the reference cup by approximately 12%.

Additionally, Table 4 shows that the peak force value of B-cup is more than that of S-cup by

approximately 70%. As previously indicated, the displacement of  $F_{\max}$  has an important role in the safety of the vehicle and its occupants. It is also clear that the peak distance of S- and B-cup with values of 22.5 and 13.1 mm, respectively, is much more than that of H- and M-tubes with an average of 1.94 and 2.06 mm which presents a benefit to the structural performance of the cups as energy absorbers. The difference in the place of formation of the first peak crush force of cups and tubes is due to the difference in the mechanism of formation of their first peak force as mentioned previously. Moreover, Table 4 demonstrates that mean crush force of B-cup (68.9 kN) is significantly greater than all other specimens, while, this value is approximately 50% greater than that of reference cup. In addition, the average value of  $F_{\text{mean}}$  of M-types (equal to 40.6 kN) and H-type tubes (equal to 37.4 kN) is less than the mean crush force of S-cup and much less than that of B-cup.

As shown in Table 4, the reference cup (S-cup) exhibits the largest value of CFE (0.688) while this value for B-cup is approximately 12% less than that of the reference cup. It is observed that M- and H-type tubes with CFE average of 0.45 and 0.43, respectively, exhibit the CFE values much less than those of S- and B-cups (0.69 and 0.61, respectively). This finding indicates that the mechanical performance, specifically in terms of CFE, of the cups outperform the tubes considered in this investigation. The experimental data summarized in Table 4 illustrate that as the viewpoint of weight reduction, the best and worst energy absorbers are  $M_{31}$  and  $H_{21}$ , respectively. Implying,  $M_{31}$  and  $H_{21}$  absorb the largest (22.7 kJ/kg) and the lowest value (13.2 kJ/kg) of energy for a given mass, respectively, as indicated in Table 4. Moreover, the B-cup illustrates an SEA less than that of the S-cup by approximately 2.7 kJ/kg. It can be noted from Table 4 indicates the stroke efficiency of B-cup is approximately 13% less than that of S-cup. It means that, with the same height, the S-cup deforms approximately 13% more than that of the B-cup. Additionally,  $M_{12}$  is the only tube which exhibited more  $S_E$  than S-cup of approximately 7% while this value for other tubes is at least 3% less than that of S-cup. The data summarized within Table 4 demonstrate that the reference cup exhibited the highest value of total efficiency while this value for the B-cup is approximately 43% less than that of the reference specimen but still larger than those of the tubes. The comparison of total efficiency between all specimens shows that the S-cup and B-cup are more effective than tubes. Moreover, similar to total efficiency, the reference specific total efficiency is the highest one of  $8.39 \text{ kg}^{-1}$ , while for the B-cup it is less than the reference one approximately 43% but unlike to  $T_E$  this value is still larger than that of  $M_{11}$ . Furthermore, for H-type tubes,  $H_{11}$  (6.57) and  $H_{32}$  (4.94) exhibit the highest and lowest values of  $T_E^*$ , respectively. The trend of  $T_E^*$  for M-type is consistent to  $T_E$  due to their same mass.

It is observed that the highest value of effectiveness factor belongs to the B-cup which is 83% more than that of S-cup. Moreover,  $H_{32}$  exhibits  $\psi$  more than the reference value (12%) while other H-type tubes possess less effectiveness factor than S-cup at least 15% (for  $H_{31}$ ). For M-type tubes, the specimen with a diameter of 51 and thickness of 1 and 1.25 mm possesses  $\psi$  less than S-cup (24% and 17%, respectively) while  $M_{12}$ ,  $M_{31}$ , and  $M_{32}$  experience more  $\psi$  than the reference value (9%, 20%, and 6%). According to the ratios of diameter to height and diameter to thickness, three deformation modes may occur in the axial compressive loading of thin-walled tubes including non-axisymmetric (diamond), axisymmetric (concertina), and a mixed mode.<sup>38</sup> As a desired design criterion, an energy absorber should deform in a repeatable and stable deformation mode under the same axial loading conditions. This criterion is used to ensure the reliability of the structure in its service.<sup>29</sup> The crushed shapes and deformed cross sections of the specimens are compared in Figures 15–17. These specimens were prepared by cutting through the post-tested specimens using a computer numeric controlled wire electrical discharge machine used by a professional machinist. It is observed that similar to  $M_{11}$ , all H-type tubes exhibited a diamond mode of deformation. On the other hand, specimen  $M_{31}$  deformed in a concertina mode, while  $M_{21}$ ,  $M_{12}$ , and  $M_{32}$  experience a mixed mode of deformation. Additionally, B- and S-cups show concertina and mixed modes, respectively. Furthermore, according to observations, B- and S-cups show repeatable behavior and therefore are more suitable for practical crashworthiness applications.

**Overall comparison.** To compare the energy absorption performance, four cases are considered in the evaluation of the mechanical behavior of these energy dissipation structures. The first case includes S-cup and  $M_{11}$  and  $M_{12}$  tubes which (with the diameter of 51

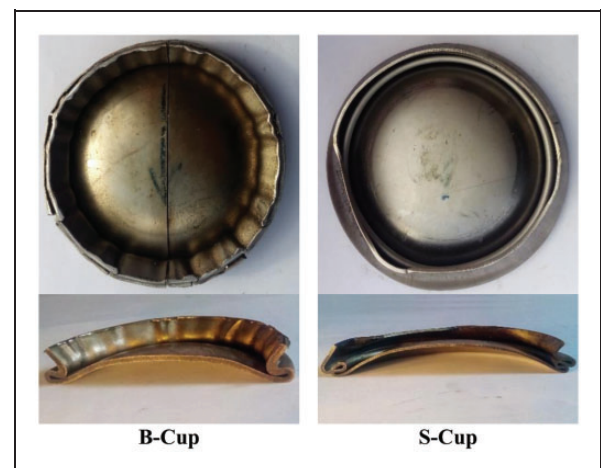


**Figure 15.** Crushed shape and cross-section of cups after the quasi-static compression test.

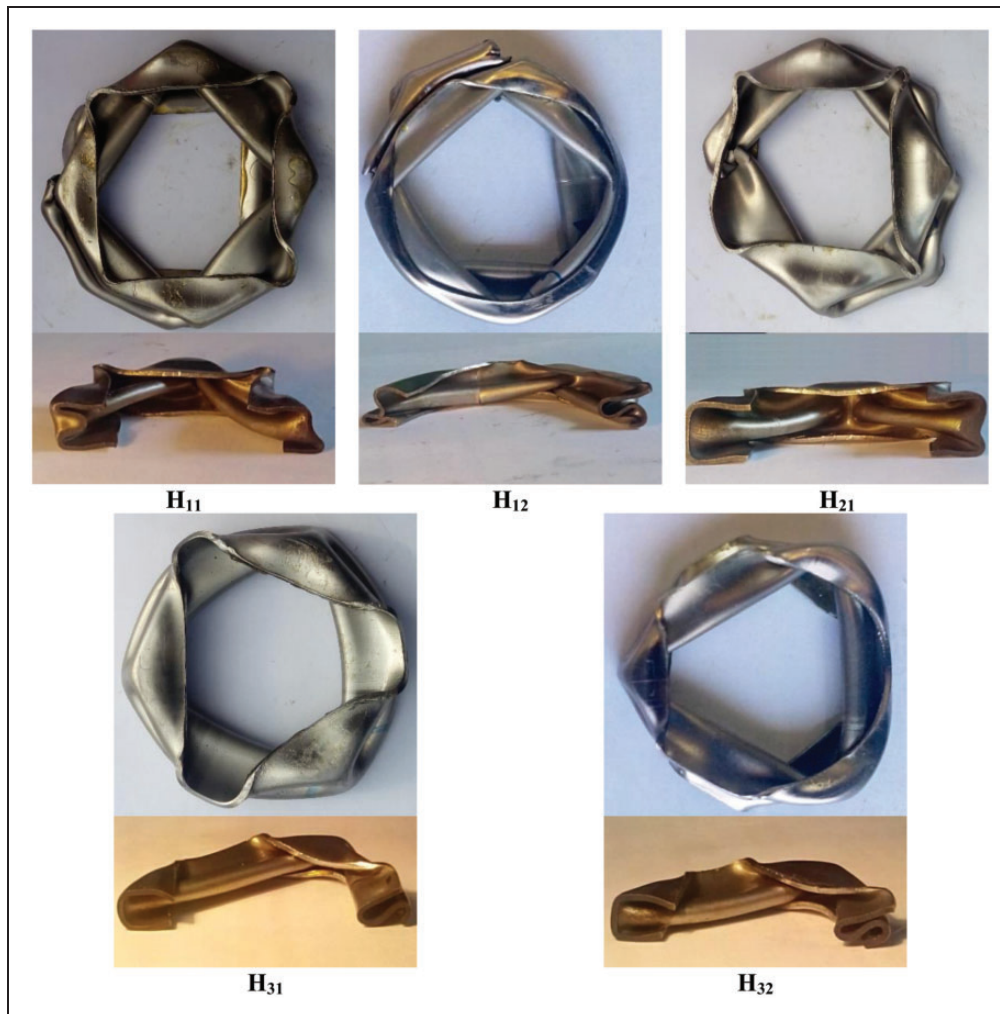


**Figure 16.** Crushed shape and cross-section of H-type tubes after the quasi-static compression test.

and 63 mm, respectively) having the same mass and thickness. The comparison of their energy absorption criteria shows that for a plate with specific mass and thickness, which geometry is more effective in energy absorption applications. Keeping in the mind that all energy absorption criteria should be at the highest value except peak crush force, and referring to Table 5, it can be concluded that the mean crushing force of the single-layer cup is 50.98% and 23.31% higher than that of  $M_{11}$  and  $M_{12}$ , respectively. Moreover, it is obvious that the cup geometry has the highest amount of total efficiency, CFE, and specific total efficiency of 0.51, 0.69, and 8.39, respectively.

Furthermore, the total energy and SEAs of S-cup are about 24.3% and 24.4% more than those of  $M_{11}$ , respectively. However, these values are 8.8% and 9.1% less than those of  $M_{12}$ , respectively. Finally, as an obvious difference between the S-cup and this type of tubes, the peak distance of the S-cup is at least 12.5 times much more than that of tubes. For the other criteria, however, the S-cup is more effective than  $M_{11}$  tube. In the second case, the cups and tubes with the same thickness and height, namely,

specimens identified as S-cup and  $H_{11}$  and  $H_{12}$  tubes are considered. These specimens can be used where space limitations are important. It is seen from Table 6 that the mean crush force of S-cup is 30.1% and 25.7% higher than those of  $H_{11}$  and  $H_{12}$ , respectively. Moreover, the total energy absorption of S-cup is 1.68 and 1.44 times of that of  $H_{11}$  and  $H_{12}$ , respectively, while comparing to  $E_{abs}$  no meaningful difference in SEA values of this case is observed. In overall, S-cup has considerably higher value than those of  $H_{11}$  and  $H_{12}$  except the peak crush force where the value of single-layer cup is approximately of 24.44% and 26.09% less than those of  $H_{11}$  and  $H_{12}$ , respectively. Finally, as in case 1, a clear difference between the peak distance of the H-type tubes and S-cup is observed here and the S-cup has the peak distance of 11 times of that of the tubes. Generally, it is evident that a single-layer cup can perform better than tubes with the same thickness and height and also tubes with the same mass and thickness under axial compression.

In the third case, a comparison between the S- and B-cups is considered. Energy absorption features of S- and B-cups are presented in Table 7. The data

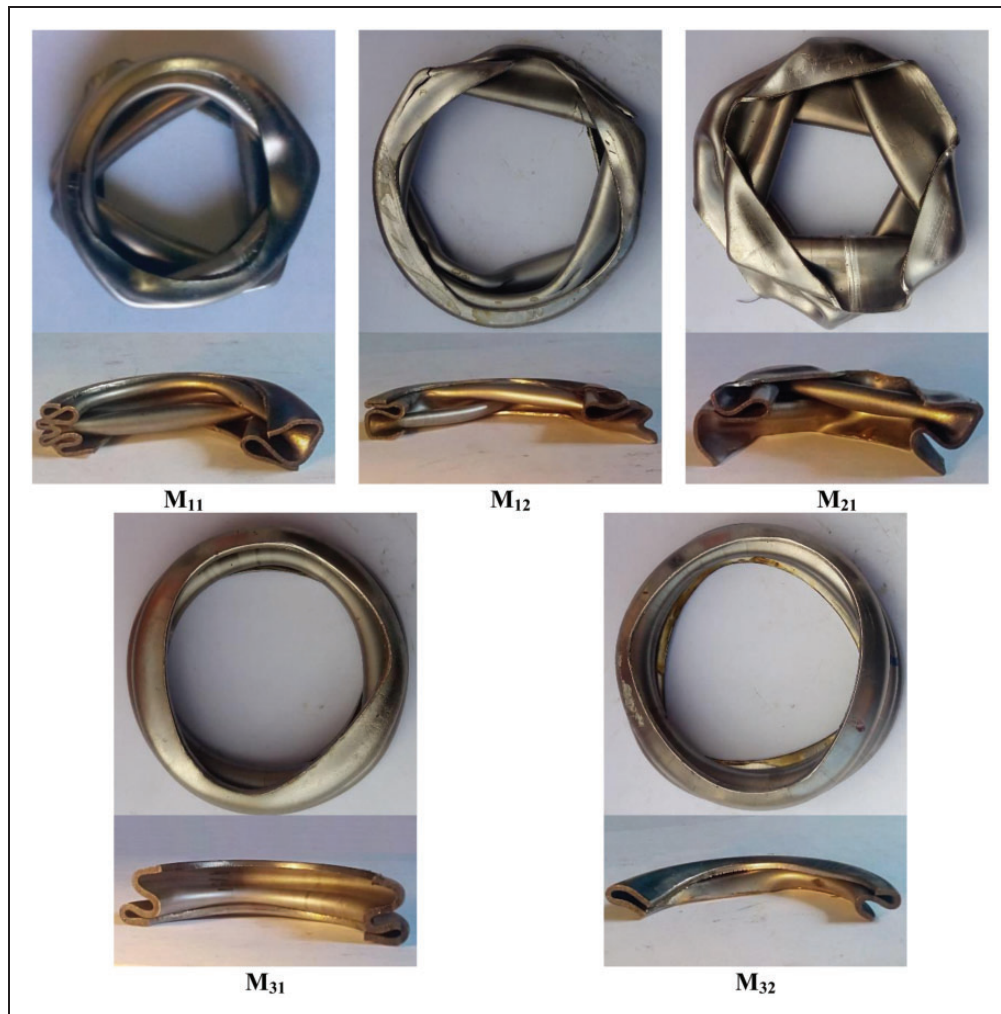


**Figure 17.** Crushed shape and cross-section of M-type tubes after the quasi-static compression test.

**Table 5.** Energy absorption features of case 1.

No.	$E_{abs}$ (kJ)	$F_{max}$ (kN)	SEA (kJ/kg)	$F_{mean}$ (kN)	$S_E$	CFE	$T_E$	$T_E^*$	$\psi$ ( $\times 10^3$ )	$\delta_p$ (mm)
S-cup	1.14	66.7	18.9	45.9	0.74	0.69	0.51	8.39	1.4	22.5
M <sub>11</sub>	0.86	57.5	14.3	22.5	0.72	0.39	0.28	4.68	1.1	1.8
M <sub>12</sub>	1.24	88.5	20.6	35.2	0.79	0.40	0.31	5.20	1.6	1.9

**Table 6.** Energy absorption features of case 2.

No.	$E_{abs}$ (kJ)	$F_{max}$ (kN)	SEA (kJ/kg)	$F_{mean}$ (kN)	$S_E$	CFE	$T_E$	$T_E^*$	$\psi$ ( $\times 10^3$ )	$\delta_p$ (mm)
S-cup	1.14	66.7	18.9	45.9	0.74	0.69	0.51	8.39	1.4	22.5
H <sub>11</sub>	0.68	83.0	18.4	32.1	0.63	0.39	0.24	6.57	0.9	1.8
H <sub>12</sub>	0.79	84.1	17.3	34.1	0.68	0.41	0.28	6.07	1.0	1.7

**Table 7.** Energy absorption features of case 3.

No.	$E_{abs}$ (kJ)	$F_{max}$ (kN)	SEA (kJ/kg)	$F_{mean}$ (kN)	$S_E$	CFE	$T_E$	$T_E^*$	$\psi$ ( $\times 10^3$ )	$\delta_p$ (mm)
S-cup	1.14	66.7	18.9	45.9	0.74	0.69	0.51	8.39	1.4	22.5
B-cup	1.33	113.1	16.2	68.9	0.64	0.61	0.39	4.75	2.7	13.0

indicate that the total absorbed energy of B-cup is of 0.19 kJ more than that of S-cup, however, its energy absorption per unit mass is approximately of 14% less than that of S-cup. Moreover, the S-cup specimens showed an averaged stroke, crush force, total, and specific total efficiencies approximately of 14%, 12%, 24%, and 43% more than those of B-cup, respectively, while its peak and mean crush force are approximately of 23 and 46 kN less than those of B-cup. Furthermore, the energy absorbing effectiveness factor of the bi-layer cup is approximately twice of that of the single-layer cup.

In the last case, to consider the mutual interactions of design variables, a comparison was carried out between S-cup and a tube with the same mass, height, and diameter as the cup. While there was no available commercial tube with the same mass, thickness, and diameter as the S-cup in the market, a numerical simulation was modeled with the same boundary condition, interaction, and mesh sizes as the FE modeling of cup. The energy absorption characteristics of this case are presented in Table 8. The data summarized in Table 8 illustrate that, the tube absorbs more energy than S-cup by approximately 81%. Furthermore, the peak crushing force of the tube is approximately 86% more than that of S-cup, while the cup exhibits more stroke efficiency than that of the tube by approximately 12%. Finally, the mean crush force of the tube is approximately twice of that of the single-layer cup.

### Numerical results

**Validation assessment.** To ensure that the proposed finite element models of the cups under quasi-static compression are sufficiently accurate, comparative studies were performed between the obtained experimental data and the FE modeling results. First, the standard error for the mean crush force is expressed in equation (17)

$$SEF_{mean} = \frac{(F_{mean})_N - (F_{mean})_E}{(F_{mean})_E} \times 100\% \quad (17)$$

where the subscripts  $E$  and  $N$  represent the experimental and numerical values, respectively. Additionally, Oberkampf and Trucano<sup>39</sup> proposed the validation metric  $V$  as presented in equation (18)

$$V = 1 - \frac{1}{L} \int_0^L \tanh \left( \left| \frac{N_{result}(\delta) - E_{result}(\delta)}{E_{result}(\delta)} \right| \right) d\delta \quad (18)$$

**Table 8.** Energy absorption features of case 4 (FE models).

No.	$E_{abs}$ (kJ)	$F_{max}$ (kN)	SEA (kJ/kg)	$F_{mean}$ (kN)	$S_E$	CFE	$T_E$	$T_E^*$	$\delta_p$ (mm)
S-cup	1.02	67.3	16.93	38.14	0.79	0.57	0.45	7.46	11.7
Tube	1.84	125.1	30.67	78.24	0.70	0.63	0.44	7.27	2.7

Moreover, the relative error is computed as mentioned in equation (19)

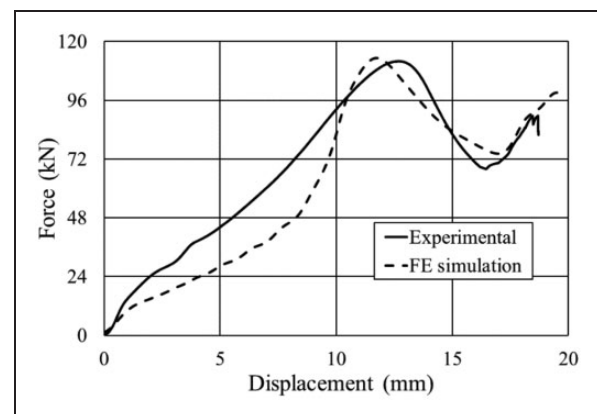
$$Error = \frac{1}{L} \int_0^L \left| \frac{N_{result}(\delta) - E_{result}(\delta)}{E_{result}(\delta)} \right| d\delta \quad (19)$$

Table 9 presents the validation analysis of the experimental findings and numerical predictions for the S- and B-cups listed. Additionally, it is essential to note that equations (18) and (19) involve the integration of the error over the displacement domain which will provide a more rigorous evaluation of error. Both equations (18) and (19) incorporate integration of the absolute value of the integrand, thus resulting in cumulative errors throughout the entire displacement range and resulting in magnitudes higher than often observed for static error measures, such as that presented in equation (17). The provided results show that the values of validation metric of energy–displacement of S- and B-cup are 87.4% and 80.7%, respectively. Moreover, Figures 18 and 19 compare the experimental and FE results of the force–displacement responses.

It is observed that the numerical results are generally, in both quantitative and qualitative assessments, adequate in predicting experimental findings. The force–displacement responses in Figures 18 and 19 illustrate

**Table 9.** FE model validation assessment by equations (17)–(19).

Specimen	SEF <sub>mean</sub> (%)	V (%)	Error (%)
S-cup	5.68	87.4	21.6
B-cup	8.84	80.7	19.9



**Figure 18.** Force/displacement response of the B-cup.

that the IPF is predicted by the FE model with a variation of 0.5%. Furthermore, in the case of S-cup, the model predicted the displacement associated with the peak force exactly, but for the case B-cup, this value was within approximately 10% error. Moreover, before the first peak force, an underestimation to the crushing force of B-cup was observed to occur. Finally, the bottom and cross-sectional views of deformed

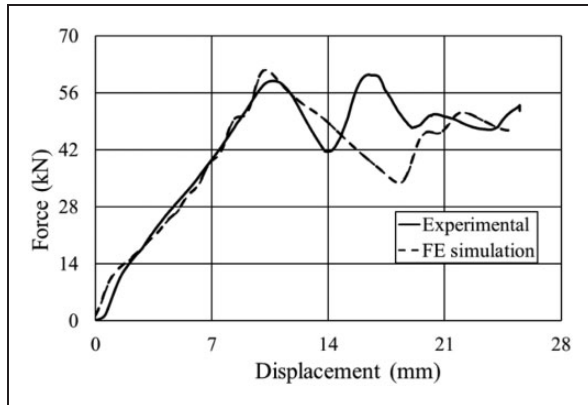


**Figure 19.** Force/displacement response of S-cup.

B- and S-cups from both experimental testing and numerical modeling predictions are presented in Figure 20. It is seen that the experimentally deformed cups are in a good similarity to the numerical results.

#### *Mechanical behavior of B-cup under compression loading.*

To study the mechanical behavior of the bi-layer cups under quasi-static compression loading, the force/displacement response of B-cup is plotted in Figure 21(a). Moreover, Figure 21(b) demonstrates photographs of the compression process for inner and outer layers. For each step, the upper and lower rows correspond to deformed shapes of outer and inner layers, respectively. Annotations in Figure 21(a) correspond to the images in Figure 21(b). Point “A” in Figure 21(a) illustrates the starting point of deformation and corresponding undeformed cup.

From these figures and force/displacement responses, it can be observed that deformation commences by an elastic deformation of the head cup up to approximately 1–2 mm of compression during loading. Accruing the deep-drawing process and springback, a curved part is developed on the head of the cup, then during the first stage, this part inverts

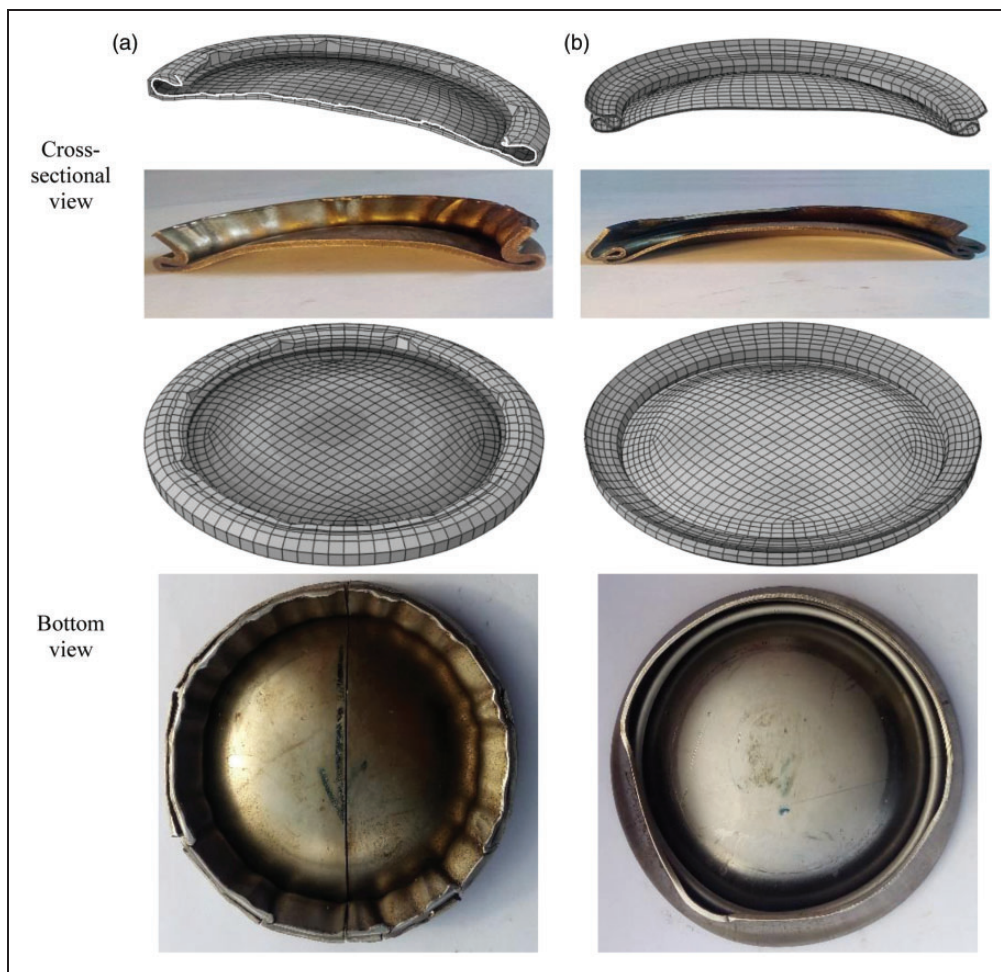


**Figure 20.** Comparison between the bottom and cross-sectional views of deformed cups resulted in the experimental process and numerical modeling: (a) B-cup and (b) S-cup.

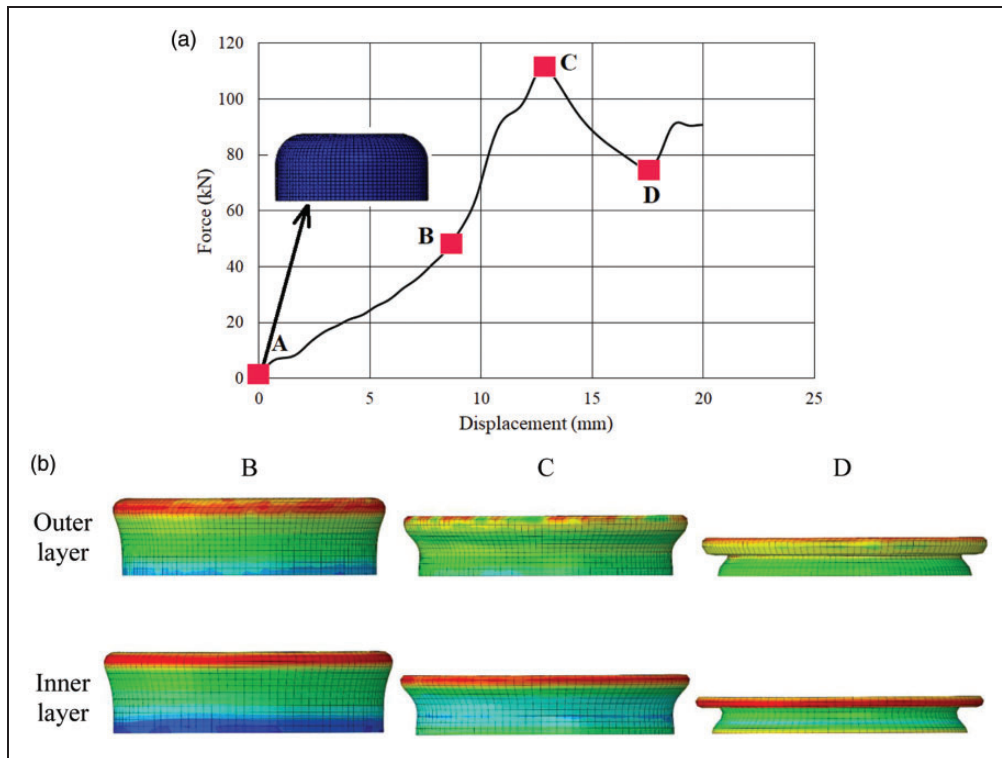


**Figure 21.** (a) Force/displacement response of B-cup. (b) Deformation steps of B-cup: the outer and inner layers.

inward and is flattened.<sup>20</sup> This deformation occurs only over a small range of compression representing approximately 10%. The following stage initiates following the elastic deformation and begins with the deformation of cup head. Previously, Ghasemabadian et al.<sup>20</sup> reported that in this stage, due to the occurrence of separation between the inner and outer layers of bi-layer cups which hold together by the adhesive, some integral numbers of lobes were formed in the cup head zone. In the case of B-cup which made by the explosive welding process and no separation is occurred, these lobes are not observed. This stage is terminated with the formation of the fold and the peak force in the head cup and force/displacement response, respectively. In the stage 2, the cup head is completely deformed and after that, no deformation in the head zone is observed. Points “B” and “C” in Figure 21(a) and (b) demonstrate the deformation of cup head and formation of the fold in the head zone, respectively. Prior to the peak force, only the head is deformed and the energy, resulting from the compressive force and platen displacement, is absorbed by this part, while deformation and energy absorption of the cup wall begin following the peak force in the stage 3. In this stage, the cup wall begins to deform at the nearest point to the cup head to either a symmetric or an asymmetric fold. Point “D” in Figure 21(a) and (b) illustrates the formed fold in the wall zone and its corresponding displacement. Finally, the cup height is compressed and folded completely and then the force rapidly increases as a

result of complete specimen compaction. Following the last stage of deformation, the cup no longer absorbs any significant amount of additional energy and full compaction occurs.

**Structural synergistic behavior of bi-layer cup.** To investigate and understand the structural synergistic behavior between the outer and inner layer of the B-cup, numerical models of standalone stainless steel and aluminum cups were developed and simulated in a fashion consistent to the scheme previously presented. The additional absorbed energy, occurring as a result of the synergistic effect, is determined using equation (20)<sup>40</sup>

$$E_{abs(Synergy)} = E_{abs(Bi-layer)} - [E_{abs(Aluminum)} + E_{abs(Steel)}] \quad (20)$$

where  $E_{abs(Synergy)}$  denotes the total absorbed energy by synergistic effect and the quantity in the square brackets demonstrates the total absorbed energy by two standalone cups. Furthermore, to achieve a better understanding of the synergistic effect, the energy/displacement responses of the B-cup and cups made of aluminum and steel are plotted in Figure 22. The figure depicts the total energy dissipation by the standalone aluminum and steel cups, the sum of these two responses and the B-cup. An increase of 49%



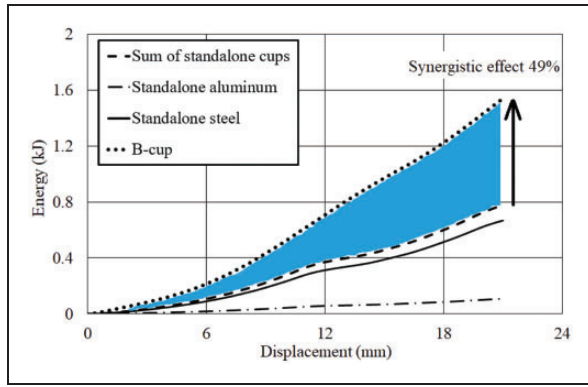


**Figure 22.** Structural synergistic effect on energy absorption capacity.

(0.76 kJ) in energy absorption more than the predicted sum of two standalone cups is illustrated.

### Optimization findings

To determine unknown coefficients of equation (15),  $3^3$  sampling points of design variables were prepared from the full factorial design method. Employing sampling points,  $3^3$  finite element simulations were carried out and their results were used to build up polynomial surface response. The polynomial response surface of the SEA and IPF of the S-cup with changing  $H$ ,  $t$ ,  $D$ , and  $r$  is demonstrated in Appendix 1. To ensure that the derived polynomial surface responses for SEA and IPF are sufficiently accurate, the relative error ( $RE$ ) between the numerical findings  $y(\chi)$  and the approximated function  $\hat{y}(\chi)$  is calculated as presented in equation (21)

$$RE = \frac{\hat{y}(\chi) - y(\chi)}{y(\chi)} \quad (21)$$

Moreover, the root mean square error (RMSE) is defined as equation (22)

$$RMSE = \sqrt{\frac{\sum_{i=1}^n (\hat{y}_i - y_i)^2}{n}} \quad (22)$$

where  $n$  is the number of validation points. The accuracies of the polynomial response surfaces are summarized in Table 10. The relative error is used to measure the local accuracy of the PRSM while the RMSE is used for measuring its global precision. It is observed that the relative errors of these functions of SEA and IPF of type 1 are less than 2.5%, while these errors for the type 2 is less than 1.5%. The small errors show that these PRSMs are accurate enough for the optimization studies. Furthermore, for type 1, RMSE values of SEA and IPF are 0.0861 and 0.1014, respectively while in the case of type 2, these values are 0.0892 and 0.1163, respectively, which show overall accuracy of the PRSMs.<sup>41</sup>

**Table 10.** Accuracies of the PRSMs of SEA and IPF.

Type		RMSE	RE (%)
1	SEA	0.0861	[-1.41, 1.18]
	IPF	0.1014	[-1.94, 2.16]
2	SEA	0.0892	[-1.54, 1.05]
	IPF	0.1163	[-0.70, 0.38]

In this study, the non-domain sorting genetic algorithm II (NSGA-II) was utilized to perform the multi-objective optimization of cup shell response under quasi-static compression loading. An in-house MATLAB<sup>®</sup> program and subroutines were coded to conduct the PRSMs as well as the NSGA-II algorithms. The provided flowchart in Figure 23 clarifies the whole design optimization procedure. Table 11 summarizes the main parameters used for NSGA-II.

Figure 24 indicates the feasible solution of the bi-objective optimization for cup shell in terms of the two crashworthiness indicators IPF and SEA of type 1, where the blue circles represent the feasible solution, while the red triangles demonstrate the Pareto frontier.

It can be seen that the feasible solution is distributed on one side of the Pareto frontier. The Pareto front provides a range of optimal solutions to help the designer to make a better decision.<sup>42</sup> Figures 25 and 26 illustrate the Pareto front of bi-objective optimization for cup shell of types 1 and 2, respectively. It is clear that two objective functions (i.e. IPF and SEA) strongly conflict with each other. This means that any further improvement in SEA must worsen IPF. In other words, an increase in the SEA leads to an undesirable increase in the IPF and vice versa, which leads to a series of solution points in the design space. Therefore, according to the Pareto front, if the energy absorption efficiency is more favorite, the bottom right region of the Pareto front can be selected as the optimal solution. On the other hand, if the IPF and safety are important to designers, the points in the top left region can be considered. Therefore, the points represented by the shape square and diamond are the single-objective optimization results of IPF and SEA, respectively. The design at diamond position can maximize the SEA while the one at square position can minimize the IPF.

Given the data in Figure 25, the optimal region for IPF is [38.85, 64.35 kN] while this region for SEA is [18.15, 33.08 kJ/kg], while these optimal regions for type 2 (Figure 26) are [40.57, 41.17 kN] and [18.55, 20.35 kJ/kg], respectively. Although the Pareto front provides a large number of optimal solutions for designers for the decision-making process, the final decision should be performed based on the most satisfactory solution (termed as “knee point”) from Pareto front.<sup>43</sup> In this study, the minimum distance selection method (TMDSM) was used to define the

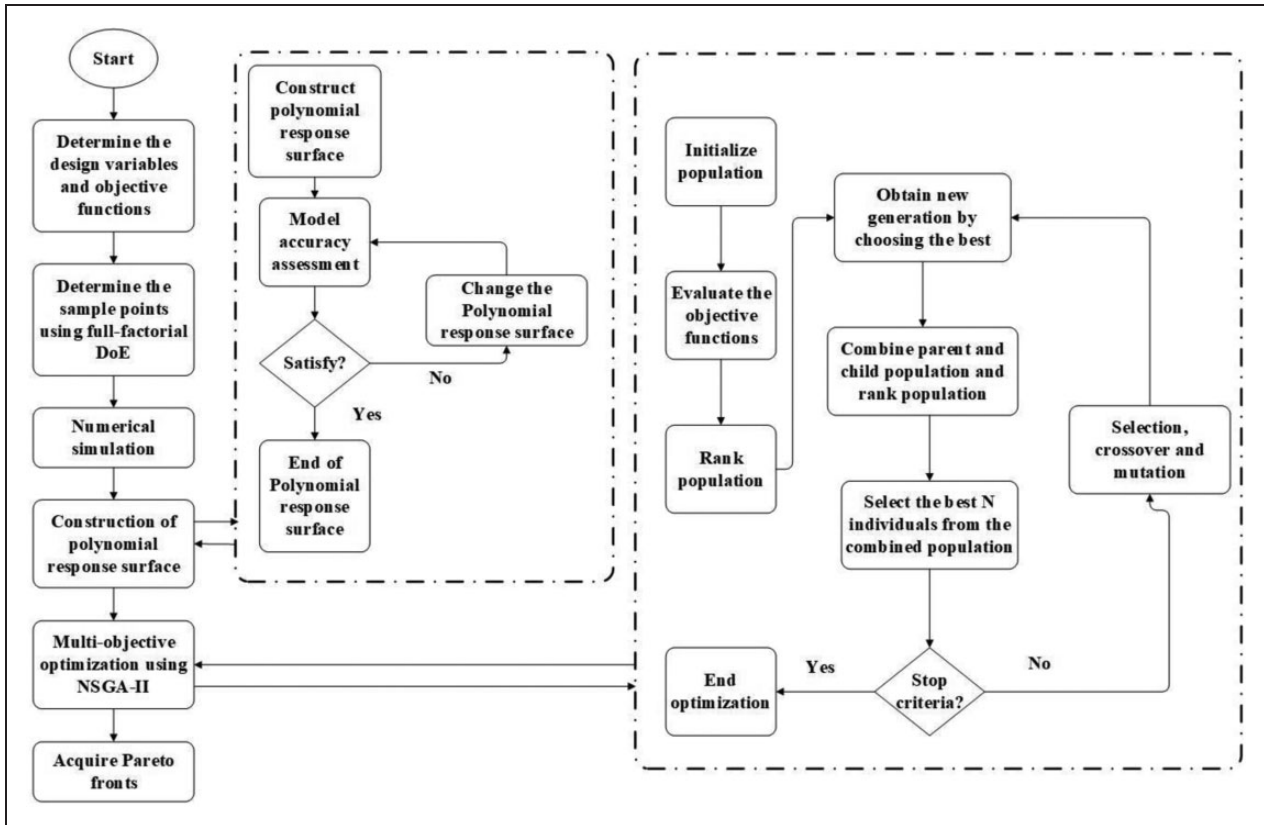


Figure 23. The flow chart of multi-objective optimization.

Table 11. Genetic algorithm parameters.

Parameter	Value
Populations size	200
Number of generations	1000
Crossing probability	0.9
Mutation probability	0.035
The total number of iterations	1000

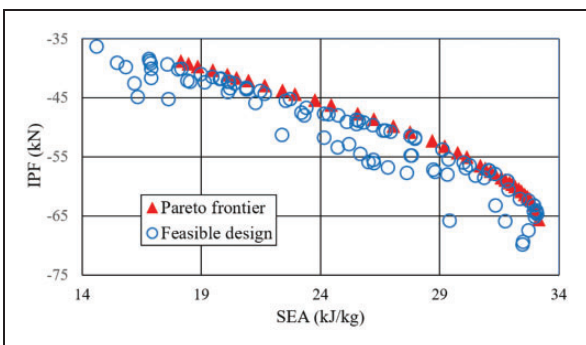


Figure 24. The feasible solution of the bi-objective optimization for S-cup shell under quasi-static compression loading.

most satisfactory solution from the Pareto front. TDMSM introduces the minimum distance between Pareto front (i.e. knee point) and an “utopia point” obtained using the optimal values of each individual

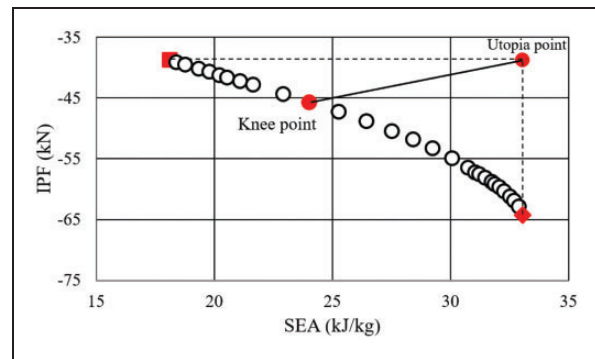


Figure 25. Pareto front of S-cup shell under quasi-static compression loading (type 1).

objective. Mathematically, the method is stated as<sup>44</sup>

$$\min D = \left[ \sum_{i=1}^m \left( f_i^k - \min(f_i) \right)^d \right]^{1/d} \quad (23)$$

where  $m$  is the number of objective functions ( $m = 2$ ),  $f_i^k$  is the  $i$ th objective value in the  $k$ th Pareto solution and  $d = 2, 4, 6, \dots$ . The obtained Knee point is the (IPF = 45.76 kN, SEA = 24.05 kJ/kg).

To ensure that the obtained designing scheme is sufficiently accurate, a comparative study was performed between the numerical modeling result and the obtained optimization data. To this end, the cup

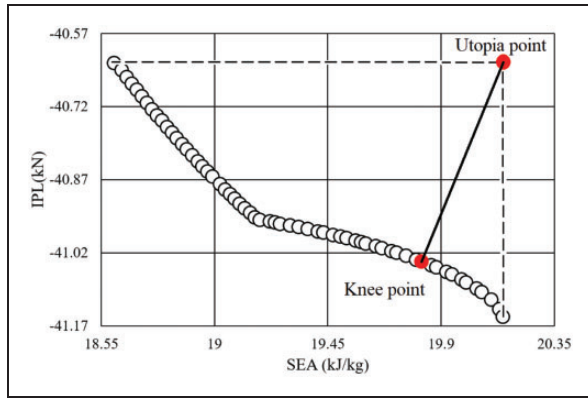


**Figure 26.** Pareto front of S-cup shell under quasi-static compression loading (type 2).

**Table 12.** Relative errors of finite element modeling and optimization values.

Type	Terms	IPF (kN)	SEA (kJ/kg)
1	Finite element modeling	42.49	21.89
	Optimization results	45.76	24.05
	Relative error (%)	7.70	9.85
2	Finite element modeling	43.98	17.92
	Optimization results	41.04	19.82
	Relative error (%)	5.55	9.59

with the dimensions corresponding to the knee points (i.e.  $D = 50$  mm,  $r_c = 14.9$  mm, and  $t = 1.09$  mm and  $D = 50$  mm,  $r_c = 8.09$  mm, and  $H = 35.80$  mm) was modeled numerically. The comparison results are summarized in Table 12. They show that in the case of type 1, the relative errors of SEA and IPF for optimization and FE modeling values are 9.85% and 7.70%, respectively, while for type 2, these error values are 9.59 and 5.55, respectively, which represent acceptable magnitudes of relative errors.

## Conclusions

In this research, the axial crush behavior and energy absorption features of single-layer cups and explosively welded bi-layer aluminum/304L stainless steel cups with those of thin-walled tubes were experimentally and numerically investigated. All specimens were subjected to quasi-static axial compression and their force/displacement responses were presented and analyzed for crashworthiness parameter determination and further assessment. A multi-objective optimization study was performed for the S-cup shell. The obtained results showed that among all studied specimens, the B-cups had the highest value of effectiveness factor. Moreover, the following points can be concluded:

- With a consistent height, the number of formed folds in the B-cup was more than that of S-cup.

In addition, the peak force of B-cup was much more than that of S-cup (at least 40%).

- M-type tubes with the thickness and diameter of 1.5 and 51 mm, respectively absorbed the most energy per unit mass (22.7 kJ/kg), while H-type tubes with the thickness and diameter of 1.25 and 51 mm, respectively had the lowest SEA of 13.2 kJ/kg.
- On the basis of space constraints, M-type tubes with the thickness and diameter of 1 and 63 mm, respectively exhibited the most stroke efficiency of 0.786 and H-type tubes with the thickness and diameter of 1.25 and 51 mm, respectively showed the least  $S_E$  of 0.60.
- Comparing CFE, the total, and the specific total efficiencies of specimens, it was observed that both B- and S-cups had larger values of CFE than other tube specimens. Moreover, total efficiencies of S-cup and B-cup were more than those of tubes (by at least  $0.39 \text{ kg}^{-1}$ ). Furthermore, the S-cup exhibited the largest value of specific total efficiency of  $8.39 \text{ kg}^{-1}$ .
- From the deformed tested specimens and the corresponding force/displacement responses, it was observed that the S- and B-cup samples showed repeatable and stable deformation behavior, hence they are good candidates for the crashworthiness applications.
- Compared to the tubes with the same thickness and height, a single-layer cup exhibited much more total energy absorption (approximately twice). Other energy absorption criteria for the S-cup were observed to be more beneficial than tubes.
- In comparison between the tubes and cups with the same mass and thickness, it was found that the total energy absorption of S-cup was twice of those of tubes. Moreover, CFE and  $F_{mean}$  of S-cup specimens were at least of 0.28 and 11.8 kN more than those of the tubes, respectively. Moreover, the S-cup specimens experienced the peak distance of 11 times of that of the tubes.
- Experimental data illustrated that the average SEA of S-cup specimens was approximately 14% more than the average value of specimens in the B-cup group. Moreover, the S-cup specimens possessed crush efficiency, CFE, total efficiency, and specific total efficiency approximately of 14%, 12%, 24%, and 43% more than those of B-cup, respectively. The energy absorbing effectiveness factor of B-cup was approximately twice of that of S-cup.
- The multi-objective optimization study showed that a single-layer cup having geometry of  $D = 50$  mm,  $r_c = 14.9$  mm, and  $t = 1.09$  mm exhibited the optimal values of IPF and SEA of 45.76 kN and 24.05 kJ/kg, respectively.
- Due to the synergistic effect, an increase of 49% (0.76 kJ) in energy absorption to that of the predicted sum of two standalone cups was observed.

## Acknowledgements

We hereby acknowledge that parts of the computation research efforts were performed on the HPC center of Ferdowsi University of Mashhad.

## Declaration of conflicting interests


The author(s) declared no potential conflicts of interest with respect to the research, authorship, and/or publication of this article.

## Funding

The author(s) disclosed receipt of the following financial support for the research, authorship, and/or publication of this article: The research documented in this manuscript has been partially funded by the Natural Science and Engineering Research Council of Canada (NSERC).

## ORCID iDs

Mohammad A Ghasemabadian  <https://orcid.org/0000-0003-2198-0346>

Mehran Kadkhodayan  <https://orcid.org/0000-0001-9880-8558>

## References

- World Health Organization. *Global status report on road safety 2018*. Geneva: World Health Organization, 2018.
- Su P-B, Han B, Yang M, et al. Axial compressive collapse of ultralight corrugated sandwich cylindrical shells. *Mater Des* 2018; 160: 325–337.
- Shariati M, Farzi G and Dadrasi A. Mechanical properties and energy absorption capability of thin-walled square columns of silica/epoxy nanocomposite. *Constr Build Mater* 2015; 78: 362–368.
- Abolfathi M, Nia AA, Attar AA, et al. Experimental and numerical investigation of the effect of the combined mechanism of circumferential expansion and folding on energy absorption parameters. *Arch Civ Mech Eng* 2018; 18: 1464–1477.
- Alkhatib SE, Tarlochan F, Hashem A, et al. Collapse behavior of thin-walled corrugated tapered tubes under oblique impact. *Thin Wall Struct* 2018; 122: 510–528.
- Yuen SC and Nurick G. The energy-absorbing characteristics of tubular structures with geometric and material modifications: an overview. *Appl Mech Rev* 2008; 61: 802–817.
- Azarakhsh S, Rahi A, Ghamarian A, et al. Axial crushing analysis of empty and foam-filled brass bitubular cylinder tubes. *Thin Wall Struct* 2015; 95: 60–72.
- Ye H, Zhou X, Ma J, et al. Axial crushing behaviors of composite pre-folded tubes made of KFRP/CFRP hybrid laminates. *Thin Wall Struct* 2020; 149: 106649.
- Arnold B and Altenhof W. Experimental observations on the crush characteristics of AA6061 T4 and T6 structural square tubes with and without circular discontinuities. *Int J Crashworthiness* 2004; 9: 73–87.
- Xu P, Yang C, Peng Y, et al. Cut-out grooves optimization to improve crashworthiness of a gradual energy-absorbing structure for subway vehicles. *Mater Des* 2016; 103: 132–143.
- Mahbod M and Asgari M. Energy absorption analysis of a novel foam-filled corrugated composite tube under axial and oblique loadings. *Thin Wall Struct* 2018; 129: 58–73.
- Wu S, Li G, Sun G, et al. Crashworthiness analysis and optimization of sinusoidal corrugation tube. *Thin Wall Struct* 2016; 105: 121–134.
- Song JF, Xu SC, Wang HX, et al. Bionic design and multi-objective optimization for variable wall thickness tube inspired bamboo structures. *Thin Wall Struct* 2018; 125: 76–88.
- Sharifi S, Shakeri M, Fakhari HE, et al. Experimental investigation of bitubal circular energy absorbers under quasi-static axial load. *Thin Wall Struct* 2015; 89: 42–53.
- Shariati M and Allahbakhsh H. Numerical and experimental investigations on the buckling of steel semi-spherical shells under various loadings. *Thin Wall Struct* 2010; 48: 620–628.
- Zhang Y, Sun G, Xu X, et al. Multiobjective crashworthiness optimization of hollow and conical tubes for multiple load cases. *Thin Wall Struct* 2014; 82: 331–342.
- Tiwari G, Khaire N, Iqbal M, et al. Ballistic response of double layered 1100-H12 aluminium hemispherical shell structure. *Thin Wall Struct* 2020; 148: 106619.
- Tasdemirci A, Sahin S, Kara A, et al. Crushing and energy absorption characteristics of combined geometry shells at quasi-static and dynamic strain rates: experimental and numerical study. *Thin Wall Struct* 2015; 86: 83–93.
- Tsukamoto H. Impact compressive behavior of deep-drawn cups consisting of aluminum/duralumin multi-layered graded structures. *Mater Sci Eng B Adv* 2015; 198: 25–34.
- Ghasemabadian M, Kadkhodayan M, Altenhof W, et al. An experimental study on the energy absorption characteristics of single-and bi-layer cups under quasi-static loading. *Int J Crashworthiness* 2018; 24: 272–285.
- Afshin E and Kadkhodayan M. An experimental investigation into the warm deep-drawing process on laminated sheets under various grain sizes. *Mater Des* 2015; 87: 25–35.
- Hanssen AG, Langseth M and Hopperstad OS. Static and dynamic crushing of circular aluminium extrusions with aluminium foam filler. *Int J Impact Eng* 2000; 24: 475–507.
- Zhang Y, Xu X, Liu S, et al. Crashworthiness design for bi-graded composite circular structures. *Constr Build Mater* 2018; 168: 633–649.
- Saboori P, Mansoor-Baghaei S and Sadegh AM. Evaluation of Head Injury Criteria under Different Impact Loading. In: *ASME 2013 International Mechanical Engineering Congress and Exposition*, 15–21 November 2013.
- Jandaghi Shahi V and Marzbanrad J. Analytical and experimental studies on quasi-static axial crush

- behavior of thin-walled tailor-made aluminum tubes. *Thin Wall Struct* 2012; 60: 24–37.
26. Lu S. *Impact energy absorption analysis of different thin-walled tubes with and without reinforcement*. Manchester, United Kingdom: The University of Manchester, 2014.
  27. Bartczak B, Gierczycka-Zbrożek D, Gronostajski Z, et al. The use of thin-walled sections for energy absorbing components: a review. *Arch Civ Mech Eng* 2010; 10: 5–19.
  28. Isaac CW and Oluwole O. Structural response and performance of hexagonal thin-walled grooved tubes under dynamic impact loading conditions. *Eng Struct* 2018; 167: 459–470.
  29. Lu G and Yu T. *Energy absorption of structures and materials*. UK: Elsevier, 2003.
  30. Jones N. Energy-absorbing effectiveness factor. *Int J Impact Eng* 2010; 37: 754–765.
  31. Meran AP. Solidity effect on crashworthiness characteristics of thin-walled tubes having various cross-sectional shapes. *Int J Crashworthiness* 2016; 21: 135–147.
  32. Fu M, Yang B and Chan W. Experimental and simulation studies of micro blanking and deep drawing compound process using copper sheet. *J Mater Process Technol* 2013; 213: 101–110.
  33. Morovvati M, Mollaie-Dariani B and Asadian-Ardakani M. A theoretical, numerical, and experimental investigation of plastic wrinkling of circular two-layer sheet metal in the deep drawing. *J Mater Process Technol* 2010; 210: 1738–1747.
  34. Goel MD. Numerical investigation of the axial impact loading behaviour of single, double and stiffened circular tubes. *Int J Crashworthiness* 2016; 21: 41–50.
  35. ASTM E9. Standard test methods for tension testing of metallic materials. In: *Annual book of ASTM standards*. West Conshohocken, PA: ASTM, 2001.
  36. Ghasemabadian M and Kadkhodayan M. Energy absorption analysis and multi-objective optimization of tri-layer cups subjected to quasi-static axial compressive loading. *Int J Eng* 2020; 33: 686–693.
  37. Nagel G. *Impact and energy absorption of straight and tapered rectangular tubes*. Brisbane, Australia: Queensland University of Technology, 2005.
  38. Andrews K, England G and Ghani E. Classification of the axial collapse of cylindrical tubes under quasi-static loading. *Int J Mech Sci* 1983; 25: 687–696.
  39. Oberkampf WL and Trucano TG. Verification and validation in computational fluid dynamics. *Prog Aerosp Sci* 2002; 38: 209–272.
  40. Wang J, Zhang Y, He N, et al. Crashworthiness behavior of Koch fractal structures. *Mater Des* 2018; 144: 229–244.
  41. Yin H, Wen G, Wu X, et al. Crashworthiness design of functionally graded foam-filled multi-cell thin-walled structures. *Thin Wall Struct* 2014; 85: 142–155.
  42. Duan S, Tao Y, Han X, et al. Investigation on structure optimization of crashworthiness of fiber reinforced polymers materials. *Composites Part B* 2014; 60: 471–478.
  43. Zhou J, Wang B, Lin J, et al. Optimization of an aluminum alloy anti-collision side beam hot stamping process using a multi-objective genetic algorithm. *Arch Civ Mech Eng* 2013; 13: 401–411.
  44. Pietrzyk M, Kuziak R, Bzowski K, et al. Material characterization for numerical simulation of manufacturing of automotive part made of magnesium alloy. *Arch Civ Mech Eng* 2020; 20: 6.

## Appendix I

### Type 1:

The polynomial response surface expression of SEA

$$\begin{aligned}
 \text{SEA}(D, t, r) = & 3.92 \times 10^1 - 1.66 \times 10^{-1}D + 6.24t \\
 & - 2.94r + 1.26 \times 10^{-2}D^2 + 2.16 \\
 & \times 10^{-1}Dt - 1.07 \times 10^{-1}Dr + 4.24 \\
 & \times 10^{-1}t^2 - 4.96 \times 10^{-1}tr + 1.02 \\
 & \times 10^{-1}r^2 - 2.75 \times 10^{-4}D^3 - 2.82 \\
 & \times 10^{-3}D^2t + 1.53 \times 10^{-3}D^2r - 6.79 \\
 & \times 10^{-3}Dt^2 + 4.08 \times 10^{-5}Dtr + 3.78 \\
 & \times 10^{-4}Dr^2 - 1.47 \times 10^{-1}Dt^3 + 4.74 \\
 & \times 10^{-2}t^2r - 7.74 \times 10^{-4}tr^2 + 3.72 \\
 & \times 10^{-3}r^3 + 1.20 \times 10^{-6}D^4 + 1.66 \\
 & \times 10^{-5}D^3t - 3.73 \times 10^{-6}D^3r - 3.45 \\
 & \times 10^{-5}D^2t^2 + 2.84 \times 10^{-5}D^2tr \\
 & - 2.04 \times 10^{-5}D^2r^2 + 3.35 \times 10^{-4}Dt^3 \\
 & + 9.14 \times 10^{-6}Dt^2r - 5.93 \\
 & \times 10^{-5}Dtr^2 + 3.13 \times 10^{-5}Dr^3 + 6.12 \\
 & \times 10^{-3}t^4 - 1.47 \times 10^{-3}t^3r - 2.28 \\
 & \times 10^{-5}t^2r^2 + 6.43 \times 10^{-5}tr^3 - 1.05 \\
 & \times 10^{-4}r^4
 \end{aligned}$$

The polynomial response surface expression of IPL

$$\begin{aligned}
 \text{IPL}(D, t, r) = & 1.33 \times 10^1 + 7.26 \times 10^{-1}D + 4.41t \\
 & - 1.32 \times 10^{-2}r - 6.18 \times 10^{-2}D^2 \\
 & + 5.48 \times 10^{-1}tr + 2.41 \times 10^{-1}r^2 \\
 & - 6.80 \times 10^{-6}D^3 - 2.11 \times 10^{-1}D^2r \\
 & - 3.09 \times 10^{-3}Dt^2 + 4.12 \times 10^{-1}Dtr \\
 & + 6.11 \times 10^{-5}Dr^2 - 1.00 \times 10^{-1}t^3 \\
 & - 4.06 \times 10^{-1}t^2r + 9.19 \times 10^{-2}tr^2 \\
 & + 3.27 \times 10^{-2}r^3 - 5.17 \times 10^{-5}D^4 \\
 & + 5.11 \times 10^{-4}D^3t + 4.50 \times 10^{-3}D^3r \\
 & + 5.18 \times 10^{-4}D^2t^2 + 3.16 \times 10^{-4}D^2tr \\
 & + 1.81 \times 10^{-5}D^2r^2 + 1.07 \times 10^{-4}Dt^3 \\
 & - 9.02 \times 10^{-5}Dt^2r - 4.56 \times 10^{-3}Dtr^2 \\
 & + 6.16 \times 10^{-5}Dr^3 - 5.03 \times 10^{-3}t^4 \\
 & + 6.72 \times 10^{-2}t^3r - 1.14 \times 10^{-2}t^2r^2 \\
 & - 8.43 \times 10^{-5}tr^3 + 7.09 \times 10^{-3}r^4
 \end{aligned}$$

**Type 2:**

The polynomial response surface expression of SEA

$$\begin{aligned}
 \text{SEA}(D, H, r) = & -1.05 - 5.24 \times 10^1 D + 1.53 \\
 & \times 10^{-3} H - 8.18r - 6.90 \times 10^{-1} D^2 \\
 & - 4.17 \times 10^{-1} DH - 1.71 \times 10^{-1} Dr \\
 & + 9.72 \times 10^{-2} H^2 - 1.01 \times 10^{-1} Hr \\
 & + 5.43 \times 10^{-1} r^2 + 4.05 \times 10^{-3} D^3 \\
 & - 1.71 \times 10^{-3} D^2 H - 6.14 \\
 & \times 10^{-2} DH^2 + 5.10 \times 10^{-4} Dr^2 \\
 & + 4.07 \times 10^{-1} DH^3 + 8.04 \\
 & \times 10^{-2} H^2 r - 8.46 \times 10^{-4} Hr^2 \\
 & - 5.19 \times 10^{-3} D^4 + 2.61 \\
 & \times 10^{-4} D^3 H + 3.41 \times 10^{-2} D^3 r \\
 & + 3.24 \times 10^{-6} D^2 Hr - 7.58 \\
 & \times 10^{-4} D^2 r^2 - 3.16 \times 10^{-6} DH^3 \\
 & + 4.18 \times 10^{-6} DH^2 r - 1.75 \\
 & \times 10^{-2} D Hr^2 + 5.14 \times 10^{-5} H^4 \\
 & + 1.06 \times 10^{-3} H^3 r - 2.46 \\
 & \times 10^{-3} H^2 r^2 + 2.12 \times 10^{-5} Hr^3 \\
 & + 1.84 \times 10^{-3} r^4
 \end{aligned}$$

The polynomial response surface expression of IPL

$$\begin{aligned}
 \text{IPL}(D, H, r) = & 1.33 \times 10^1 + 7.41 \times 10^{-1} D + 1.90 \\
 & \times 10^{-1} r - 2.38 \times 10^{-2} D^2 + 1.84 DH \\
 & + 7.68 \times 10^{-2} Dr + 7.26 \times 10^{-1} H^2 \\
 & + 2.33 \times 10^{-1} Hr + 6.49 \times 10^{-3} r^2 \\
 & + 4.31 \times 10^{-4} D^3 - 1.39 \times 10^{-3} D^2 r \\
 & + 9.42 \times 10^{-3} DH^2 + 2.55 \\
 & \times 10^{-4} D Hr + 5.65 \times 10^{-5} Dr^2 \\
 & + 1.60 \times 10^{-2} Hr^2 - 4.52 \times 10^{-3} r^3 \\
 & - 1.25 \times 10^{-6} D^4 - 3.3 \times 10^{-5} D^3 H \\
 & + 2.14 \times 10^{-6} D^3 r + 1.52 \\
 & \times 10^{-4} D^2 H^2 - 9.37 \times 10^{-4} DH^3 \\
 & - 1.10 \times 10^{-5} DH^2 r - 1.50 \\
 & \times 10^{-6} D Hr^2 - 2.09 \times 10^{-5} Dr^3 \\
 & - 4.50 \times 10^{-3} H^4 + 1.98 \times 10^{-3} H^3 r \\
 & + 2.83 \times 10^{-4} H^2 r^2 - 2.39 \\
 & \times 10^{-4} Hr^3 + 8.53 \times 10^{-5} r^4
 \end{aligned}$$